Eidgenössische Technische Hochschule Zürich
Swiss Federal Institute of Technology Zurich

Trapped Ion Quantum Information

Design and Implementation of an Optical Tweezer Setup for Calcium Atoms

Master's Thesis

Qianlong He
heqian@ethz.ch

Trapped-Ion Quantum Information Group
Department of Physics, D-PHYS
ETH Zürich

Supervisors:
Silvan Koch, Wojciech Adamczyk, Dr. Claudia Politi, Dr. Daniel Kienzler,
Prof. Dr. Jonathan Home

October 18, 2024

Acknowledgements

I would like to express my deepest gratitude to everyone who supported me throughout this project.

First, I want to thank the Rydberg group. When I started my Master's thesis, I had no experience with optics, but your incredible support helped me overcome challenges and complete this project. A special thanks to Claudia for always being so responsible, patient, and approachable. Thank you for teaching me your professional experimental techniques, answering my questions so clearly, helping me with machine parts in the workshop, and always being happy to hear about my progress. Silvan, I really appreciate your clear and insightful guidance on optics, the SLM, and Zemax, it has been a huge help. I'm also grateful to Wojciech for his enthusiastic advice and inspiration, which kept me motivated throughout. Thanks to Pavel for always answering my curious questions about your fascinating project.

My thanks go to Prof. Dr. Jonathan Home and Dr. Daniel Kienzler for giving me the opportunity to conduct my Master's thesis at the TIQI group and for posing thought-provoking questions and providing insightful instructions during weekly meetings.

A special thanks to the people in B25 and B18. David, Fabian, Moritz, Flo, and Kai, thank you for your warmth and company during the days I spent in the lab. You guys created a nice atmosphere and chill vibe.

I would also like to thank Gillen for his help with the microscope, and Matteo, Yingying, and Henrik for sharing their fascinating research. To the entire TIQI group, your collective brilliance made this experience truly memorable.

Finally, I extend my thanks to my family and friends for their support.

Abstract

Neutral atom-based quantum computing requires precise isolation and confinement of individual atoms. Optical tweezers, which consist of highly focused laser beams, provide this capability by creating a dipole potential to the atoms. This project uses 532 nm laser light together with the liquid crystal spatial light modulator (LC SLM) to generate an optical tweezer array for trapping Ca^{40} atoms. We first present the design and implementation of the experimental setup, which is compatible with the existing Magneto-Optical Trap (MOT) setup. We then investigate the effects of various experimental components on the tweezer waist size (around 1.2 μm) and demonstrate two methods for tuning the tweezer focal plane. Additionally, we propose an approach to correct the tweezer array aberrations using an indirect wavefront calibration (WFC) and analyze the aberrations introduced by individual setup components.

Contents

Chapter 1

Introduction

Quantum computing stands as one of the foremost technological advancements of the 21st century, holding the potential to revolutionize diverse fields, including cryptography [1], molecule science [2], and complex simulations [3]. By harnessing the quantum properties of superposition and entanglement, quantum computers can perform certain types of calculations exponentially faster than classical computers [4]. Among the leading candidates for implementing scalable quantum systems, neutral atoms have emerged as a highly promising candidate for building the quantum processing unit owing to their properties of being inherently identical and easy to scale up [5].

Rydberg atoms [6], of which a valence electron is excited to a large principal quantum number state, are widely explored in neutral atom-based quantum computing. The long cation-electron distance gives rise to exaggerated properties such as large electric dipole moments, making the Rydberg atoms particularly attractive due to their long-range dipole-dipole interactions. Those interactions enable the entangling operations between distant atoms, which are crucial for building two-qubit quantum gates [7, 8]. However, the lifetime of these low-angular momentum states is limited to tens of microseconds, posing some limitations to the achievable two-qubit gate fidelities. Circular Rydberg atoms, of which the valence electron is excited to the maximum orbital angular momentum Rydberg states, serve as a possible solution due to their longer lifetimes. Possessing only a single radiative decay pathway [9], these states can achieve a lifetime of up to 10 ms in cryogenic conditions. The lifetime can be further extended inside a cavity that suppresses the local density of states at the transition frequency [10, 11]. In addition, the circular Rydberg state of alkaline earth atoms is a promising candidate for quantum non-destructive readout techniques and coherent manipulation [12, 13].

On the other hand, Rydberg atoms also offer a unique advantage in overcoming the limitations of scalability and connectivity. Since there are only weak magnetic dipole-dipole and Van der Waals interactions between ground-state atoms, it is possible to closely trap many atoms on a large scale. Optical tweezers have emerged as an efficient tool for this purpose. By using highly focused laser beams, optical tweezers can trap and manipulate individual neutral atoms with great precision, providing the necessary tools for building a logical quantum processor based on programmable atom arrays [14, 15].

This thesis focuses on building an optical tweezer setup for trapping calcium atoms in a room-temperature experimental apparatus. The structure of the thesis is as follows:

1. **Chapter 2** encompasses the necessary theories of this work. It shows the wave propagation theory through a Fourier lens, which serves as a basis for understanding

the formation of the tweezer array. It also includes a discussion about aberrations and Zernike polynomials, which are metric and useful tools for assessing the performance of the optical system.

2. **Chapter 3** is dedicated to the key ingredient of the experimental setup, the spatial light modulator (SLM). It first briefly presents the internal structure and working mechanism of the SLM. Then it discusses various calibrations of the SLM, for instance, the phase calibration, the Fourier calibration, and the wavefront calibration.

3. **Chapter 4** shows the design and implementation of the experimental setup. It explains how the setup combines the tweezer light and Magneto-Optical Trap (MOT) light to overcome the challenge caused by the limited number of viewports.

4. **Chapter 5** presents all the characterizations and tests of the setup. It introduces two methods to measure the tweezer waist size and investigates the influence of various components on the tweezer waist. Then it proposes two approaches to shift the focus of the tweezer arrays. It also studies the possibility of correcting the tweezer aberration by performing an indirect wavefront calibration. Ultimately, it analyzes each optical component's aberration by its wavefront map.

Chapter 2

Theory

2.1 Wave propagation theory

The realization of the optical tweezer involves achieving a specific light structure within the trapping region. The optical tweezer's theoretical foundation is based on Fourier optics principles. This section first introduces wave propagation in the classic case where light is propagating through a lens. In the second case, an additional Keplerian telescope is introduced, which modifies the result obtained in the former case.

2.1.1 Wave propagation through a lens

Following Ref. [16, 17], one can relate the input field $E_d(x', y')$ (as shown in Fig. 2.1) on the object plane located at a distance d before the lens (with focal length f), to the output field $E_z(x, y)$ at the image plane located a distance z after the lens by using the following equation:

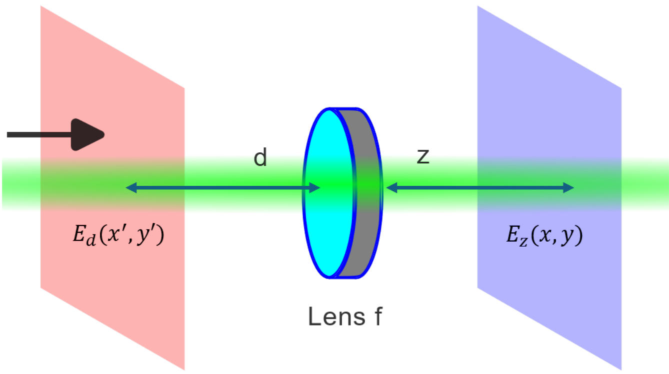

Figure 2.1: Wave propagation through a lens. The input field $E_d(x', y')$ is propagating from the object plane, located at a distance d from the lens (with focal length f) to the output field $E_z(x, y)$ on the image plane, located at a distance z from the lens.

$$E_z(x, y) = \frac{i}{\alpha} \int dx'dy' E_d(x', y') e^{\frac{ik}{2F}(x'^2+y'^2)} \exp\left\{2\pi i(x'x + y'y)\frac{1}{\alpha}\right\}, \tag{2.1}$$

where α is a scaling factor of the Fourier transform, defined as:

$$\alpha = \lambda(d - \frac{dz}{f} + z), \tag{2.2}$$

and F is the effective focal length of a virtual lens, given by:

$$\frac{1}{F} = \frac{1}{d} - \frac{1}{d^2(z^{-1} - f^{-1} + d^{-1})}. \tag{2.3}$$

In the optical tweezer setup, the object plane coincides with the Fourier lens, i.e. $d = 0$, thus Eq. 2.1 can be simplified to:

$$E_z(x, y) = \frac{i}{\lambda z} \int dx' dy' E_d(x', y') \exp\{2\pi i(x'x + y'y)/(\lambda z)\}. \tag{2.4}$$

There are two cases for the image plane distance z:

- **Case 1: Image Plane Coincides with Focal Plane ($z = f$):**

  When the image plane is located at the focal plane of the lens ($z = f$), the Eq. 2.4 reduces to:

  $$E_z(x, y) = \frac{i}{\lambda f} \int dx' dy' E_d(x', y') \exp\{2\pi i(x'x + y'y)/\lambda f\}. \tag{2.5}$$

  This result shows that the field in the lens focal plane $E_z(x, y)$ is the Fourier transform of the input field $E_d(x', y')$, evaluated at the spatial frequency $(\frac{x}{\lambda f}, \frac{y}{\lambda f})$. To verify this, consider a plane wave propagating at an angle θ with respect to the optical axis. Let the wave number vector of the input beam be $\vec{k}$. For simplicity, assume its projection in the x-direction is $k \sin\theta = \frac{2\pi}{\lambda} \sin\theta$, and no component is in the y-direction. In the (x, y)-plane, the field has a spatial frequency $(\frac{\sin\theta}{\lambda}, 0)$. From Eq. 2.5, we identify $x/\lambda f = \sin\theta/\lambda$ and $y/\lambda f = 0$. It indicates that the field in the image plane is located at the coordinates $(f \sin\theta, 0)$. This result is consistent with the result from geometric optics $(f \tan\theta, 0)$ in the paraxial approximation where $\sin\theta = \tan\theta$.

- **Case 2: Image plane out of Focal Plane ($z \neq f$):**

  When the image plane is out of the lens focal plane, consider $z = f + \delta z$ where δz is the out-of-focus amount. Eq. 2.4 becomes:

  $$E_z(x, y) = \frac{i}{\lambda(f + \delta z)} \int dx' dy' E_d(x', y') e^{-i\frac{2\pi}{\lambda(f+\delta z)}(x'x+y'y)} e^{-i\frac{\pi\delta z}{\lambda f(f+\delta z)}(x'^2+y'^2)}. \tag{2.6}$$

  Compared to the first case, an additional phase factor $e^{-i\frac{\pi\delta z}{\lambda f(f+\delta z)}(x'^2+y'^2)}$ appears in the Fourier transform. The spatial frequency at which the Fourier transform is evaluated is also slightly modified due to δz. When $\delta z \ll f$, the factor $f + \delta z$

can be approximated by f. Under this assumption, the additional phase factor can be canceled by imprinting a compensating phase $\phi = \frac{\pi\delta z}{\lambda f^2}(x'^2 + y'^2)$ to the input field, and the output field $E_z(x, y)$ becomes identical to that in the first case. This indicates that the focal plane is shifted by δz.

2.1.2 Wave propagation through a Keplerian telescope

In the optical tweezer setup, a Keplerian telescope is used to expand the initial field before it reaches the Fourier lens. The magnified image is used as the input field for the object plane of the lens (see Fig. 2.2). If the telescope magnification is $-M$, (the negative sign corresponds to the inverted image), the field relationships are as follows:

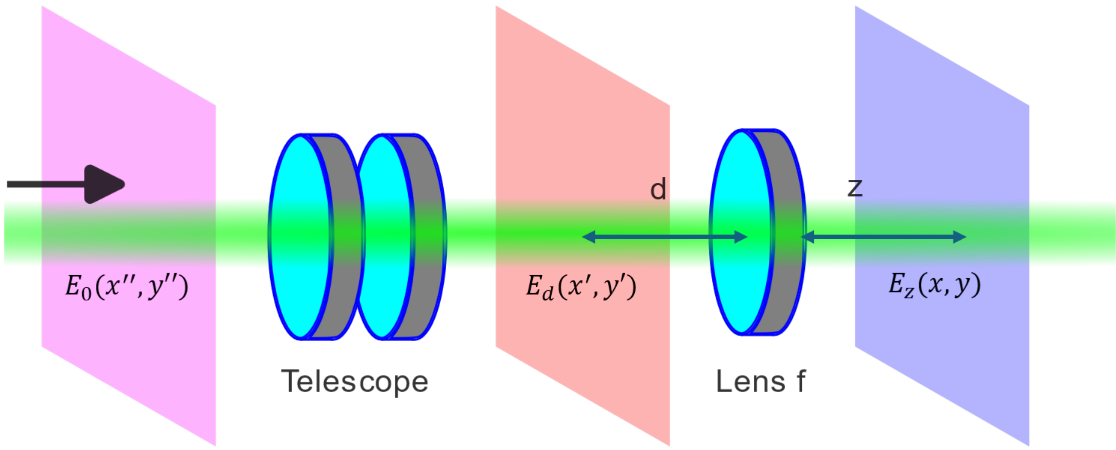

Figure 2.2: Wave propagation through a Keplerian telescope and a lens. The input field $E_0(x'', y'')$ is first magnified by a Keplerian telescope, and the field after magnification $E_d(x', y')$ serves as the input of the Fourier lens.

For conjugate points (x'', y'') and (x', y'), the coordinate transformation and field correspondence are given by

$$x' = -Mx'' \quad y' = -My'', \tag{2.7}$$

$$E_o(x'', y'') = ME_d(x', y'). \tag{2.8}$$

Substituting this into Eq. 2.1, we obtain:

$$E_z(x, y) = \frac{i}{\alpha} \int M dx'' dy'' E_0(x'', y'') e^{\frac{ikM^2}{2F}(x''^2 + y''^2)} e^{-2\pi i M(x''x + y''y)/\alpha}. \tag{2.9}$$

The telescope introduces a factor $-M$ to the spatial frequency at which the Fourier transform is evaluated:

$$f_x = (\frac{x}{\lambda f}) \rightarrow f'_x = (\frac{-Mx}{\lambda f}), \tag{2.10}$$

$$f_y = (\frac{y}{\lambda f}) \rightarrow f'_y = (\frac{-My}{\lambda f}). \tag{2.11}$$

As mentioned in the case $z \neq f$, a phase ϕ applied on the input field can compensate for the additional phase factor in the Fourier transform. The phase ϕ must also account for this magnification:

$$\phi = -\frac{\pi \delta z}{\lambda f^2}(x''^2 + y''^2) \rightarrow \phi' = -\frac{\pi \delta z M^2}{\lambda f^2}(x''^2 + y''^2). \tag{2.12}$$

Compared to the case without a telescope, the Fourier transform is inverted along the x axis and scaled down by a factor of M, while the field amplitude is magnified by a factor of M.

In conclusion, the field at the focal plane of a lens is the Fourier transform of the input field. A phase mask can be applied to the input field to effectively shift the focal point into the image plane. When a Keplerian telescope is used prior to this configuration, a factor of $-M$ must be accounted for in the field transform equations.

2.2 Aberrations

In an ideal optical system, image quality is limited only by the wave nature of light, corresponding to the diffraction-limited regime. However, in practical experimental setups, image quality is often degraded by aberrations caused by deviations from idealized imaging conditions, such as the thin-lens approximation or paraxial approximation. This section first introduces some common types of aberrations, followed by a discussion of a useful tool for analyzing aberrations: the Zernike polynomials.

2.2.1 Common types of optical aberrations

Aberrations in optical systems can take several forms, with the most common being spherical aberration, coma, and astigmatism [18].

- **Spherical aberration [18, 19]**: Spherical aberration occurs when the rays of a light source passing through a spherical surface focus at different points, causing a blurred image. Fig. 2.3 illustrates the refraction of light through a spherical surface with radius R, where n_1 and n_2 are the refractive indices of the respective media. A ray originating from a point source S strikes the spherical surface at point A and is refracted to form an image at point P on the optical axis. By applying Fermat's Principle, the object and image distances s_o, s_i are related by the following equation:

$$\frac{n_1}{l_0} + \frac{n_2}{l_i} = \frac{1}{R}\left(\frac{n_2 s_i}{l_i} - \frac{n_1 s_o}{l_o}\right). \tag{2.13}$$

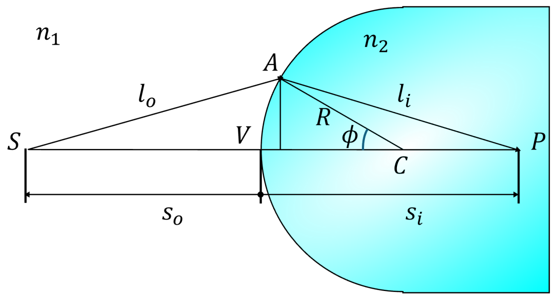

Figure 2.3: Refraction by a spherical surface for the rays coming from a point source S. The center of the sphere is at C, and its radius is R. n_1 and n_2 are the corresponding refractive index for the left and right medium. The ray strikes on the surface at point A, it is refracted and crosses the optical axis at point P.

The paraxial approximation assumes that the angle ϕ between the line AC and the optical axis is small, i.e. A is close to V, such that the treatment of $\sin\phi = \tan\phi = \phi$ and $\cos\phi = 1$ is valid, which is usually called the first-order theory. Under this condition, $l_o \approx s_o$ and $l_i \approx s_i$, and Eq. 2.13 simplifies to:

$$\frac{n_1}{s_o} + \frac{n_2}{s_i} = \frac{n_2 - n_1}{R}. \tag{2.14}$$

However, when ϕ is large, the treatment $\sin\phi\ = \phi$ is not accurate anymore. To have a better approximation, we retain the first two terms in the expansion

$$\sin\phi = \phi - \frac{\phi^3}{3!} + \frac{\phi^5}{5!} - \frac{\phi^7}{7!} + \cdots, \tag{2.15}$$

where we have the so-called third-order theory. The object and image conjugation relation 2.13 becomes

$$\frac{n_1}{s_o} + \frac{n_2}{s_i} = \frac{n_2 - n_1}{R} + h^2\left[\frac{n_1}{2s_0}\left(\frac{1}{s_o} + \frac{1}{R}\right)^2 + \frac{n_2}{2s_i}\left(-\frac{1}{s_i} + \frac{1}{R}\right)^2\right], \tag{2.16}$$

where h represents the height from A to the optical axis. Note that the h^2-dependent term in Eq. 2.16 is positive. Therefore, for a fixed object distance s_o, an increase in h results in a corresponding decrease in image distance s_i. This indicates that rays passing through a surface point A father from the optical axis are refracted more strongly, causing the image to form closer to the surface. Conversely, rays passing through a surface point A closer to the optical axis form an image at a greater distance. This effect also applies to lenses, as illustrated in Fig. 2.4, where a collimated light is perpendicularly shining on the lens. For rays passing through the edge of the lens are diffracted more and have a shorter focal length than those passing through the center.

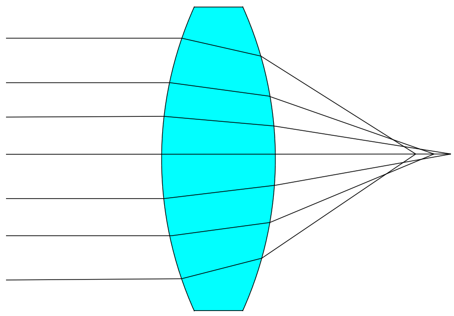

Figure 2.4: Spherical aberration: Collimated light passes through a convex lens. Light rays entering closer to the center of the lens and those passing near the edge converge to different points, resulting in a blur of image.

- **Coma [20]**: Coma is an optical aberration that manifests as asymmetric, comet-like distortions in the images of off-axis point sources. As shown in Fig. 2.5, rays from an off-axis point source pass through a convex lens, forming multiple cones of rays, each represented by a different color. These cones of rays, depending on their radial distance from the center of the lens, focus at different points.

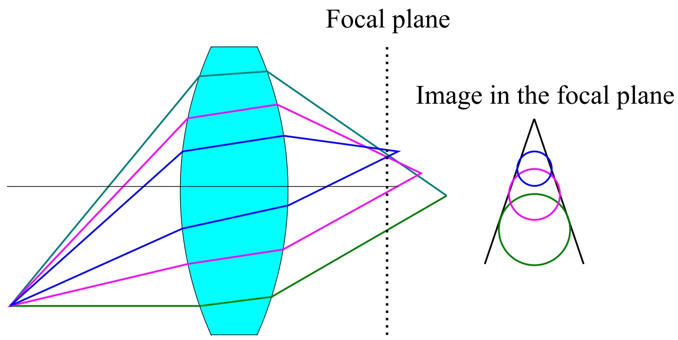

Figure 2.5: Coma aberration: Light from an off-axis point source passes through a convex lens. Each circular cone of rays (represented by different colors) is focused at different locations. In the focal plane, the inner rays form smaller, sharper rings, while the marginal rays form larger, displaced rings, leading to asymmetric distortion in the image.

The right part of Fig. 2.5 illustrates the formed image in the focal plane. Inner rays, which are closer to the optical axis, form smaller, sharper circles, while marginal rays, which are farther from the optical axis, form larger, displaced rings. This misalignment of focus points results in the characteristic comet-like tail in the image, where intensity gradually decreases from a bright core toward the edges. The effect becomes more pronounced as the object displacement from the optical axis increases, causing the image to stretch and blur asymmetrically in the direction of the off-axis source.

- **Astigmatism**: Astigmatism is an optical aberration where rays in different meridians (tangential and sagittal planes) focus at different points. This typically happens when an object is significantly off-axis, causing rays in the tangential and sagittal planes to encounter different lens curvatures (see Fig. 2.6). Due to this asymmetry, the rays in the two planes focus at different points. This separation of focal points leads to an inability to bring both planes into sharp focus simultaneously, which is a key characteristic of astigmatism.

  Another contributing factor to astigmatism is lens asymmetry, where the lens has different refractive indices across its surface due to manufacturing imperfections or design choices. This also results in a difference in focus between rays from the tangential and sagittal planes even for an on-axis object.

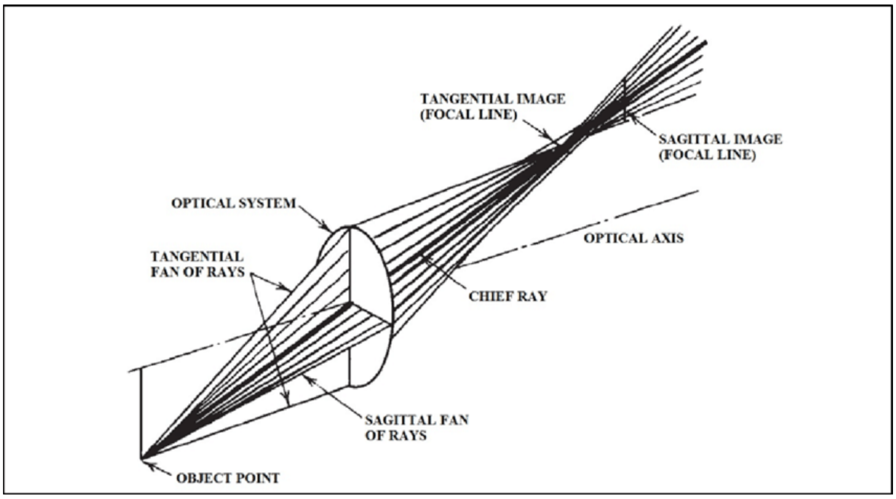

Figure 2.6: Astigmatism in an optical system. Incident tangential and sagittal rays focus at different planes, causing distortion. Figure adapted from [21].

There are also other types of aberrations like field curvature and distortion, one can refer to Ref. [18] for more details.

2.2.2 Aberrations and Zernike polynomials

Aberrations can be considered in terms of rays as described above, it can also be interpreted in terms of the wavefront. The wavefront is the collection of points that share the same optical path from the light source [22]. For example, the wavefront of a collimated light is ideally assumed to be a plane, and the wavefront of a converging beam is supposed to be a sphere. However, in the experiment, due to the wavefront distortion introduced by the aberration of optical elements, the wavefront is typically different from the idealized case. Therefore, the wavefront is an important metric to evaluate the amount of aberrations present in an optical system.

Zernike polynomials were named after the Dutch physician, Fritz Zernike, and consist of an infinite number of polynomials that are orthogonal and continuous over a unit circle [23]. They are regarded as a useful mathematical tool to describe the wavefront of an optical system. Considering a wavefront function in polar coordinate r, θ, denoted by $W(r, \theta)$. It can be expressed as [24]:

$$W(r, \theta) = \sum_{j}^{\infty} C_j Z_j(r, \theta), \tag{2.17}$$

where C_j are the coefficients of each polynomial indicating the magnitude of each type of Zernike aberration present in the wavefront aberration map, and Z_j are the Zernike polynomials. The Zernike polynomials are defined as:

$$Z_j(r, \theta) = Z_n^m(r, \theta), \tag{2.18}$$

$$Z_n^m(r, \theta) = N_n^m R_n^m(r) \cos m\theta, \tag{2.19}$$

$$Z_n^{-m}(r, \theta) = N_n^m R_n^m(r) \sin m\theta. \tag{2.20}$$

where n and m are non-negative integers and satisfy $n - m \geq 0$ and $n - m =$ even. There are multiple schemes of relate the index j with the indices n and m: Noll indexing scheme, OSA/ANSI indexing scheme, Fringe indexing scheme, and Born and Wolf indexing scheme [25]. Here we only present the Noll scheme, which is given by:

$$j = \begin{cases} \frac{n(n+1)}{2} + 1 & \text{if } m = 0, \\ \lfloor \frac{n(n+1)}{2} + m, \frac{n(n+1)}{2} + m + 1 \rfloor & \text{if } m \neq 0, \end{cases} \tag{2.21}$$

where $\lfloor x \rfloor$ denotes the floor function that returns the smallest integer that is small or equal to x.

$R_n^m(r)$ is a radial function defined as:

$$R_n^m(r) = \sum_{l=0}^{(n-m)/2} \frac{(-1)^l (n-l)!}{l![\frac{1}{2}(n+m) - l]![\frac{1}{2}(n-m) - l]!} r^{n-2l}, \tag{2.22}$$

and the normalization factor N_n^m is defined as:

$$N_n^m = \left(\frac{2(n+1)}{1 + \delta_{m0}} \right)^{1/2}, \tag{2.23}$$

where δ_{m0} is the Kronecker delta function.

The normalization and orthogonality are formulated as:

$$\frac{\int_0^{2\pi}\int_0^1 Z_j(r,\theta)Z_{j'}(r,\theta)r\mathrm{d}r\mathrm{d}\theta}{\int_0^{2\pi}\int_0^1 r\mathrm{d}r\mathrm{d}\theta} = \delta_{jj'}. \tag{2.24}$$

From which we have the following results:

- **Coefficient extraction**:

$$C_j = \frac{1}{\pi}\int_0^{2\pi}\int_0^1 W(r,\rho)Z_j(r,\theta)r\mathrm{d}r\mathrm{d}\theta, \tag{2.25}$$

- **Wavefront mean value**:

$$\overline{W(r,\rho)} = \frac{1}{\pi}\int_0^{2\pi}\int_0^1 W(r,\rho)r\mathrm{d}r\mathrm{d}\theta = C_0, \tag{2.26}$$

- **Wavefront square mean value**:

$$\overline{W^2(r,\rho)} = \frac{1}{\pi}\int_0^{2\pi}\int_0^1 W^2(r,\rho)r\mathrm{d}r\mathrm{d}\theta = \sum_{j=0}^{\infty} C_j^2, \tag{2.27}$$

- **Wavefront variance**:

$$\sigma^2 = \overline{W^2(r,\rho)} - (\overline{W(r,\rho)})^2 = \sum_{j=1}^{\infty} C_j^2. \tag{2.28}$$

Tab. 2.1 lists the first 15 terms of the polynomials in the polar coordinate and the values for n, m, and j. Fig. 2.7 shows the pyramid of the non-normalized Zernike circle polynomials up to the sixth degree under the Noll indexing scheme.

j	n	m	$Z_j(\theta,\rho)$	Aberration
1	0	0	1	Piston
2	1	1	$2\rho\cos\theta$	x-tilt
3	1	1	$2\rho\sin\theta$	y-tilt
4	2	0	$\sqrt{3}(2\rho^2-1)$	Defocus
5	2	2	$\sqrt{6}\rho^2\sin 2\theta$	Oblique astigmatism
6	2	2	$\sqrt{6}\rho^2\cos 2\theta$	Vertical astigmatism
7	3	1	$\sqrt{8}(3\rho^2-2\rho)\sin\theta$	Primary y-coma
8	3	1	$\sqrt{8}(3\rho^2-2\rho)\cos\theta$	Primary x-coma
9	3	3	$\sqrt{8}\rho^3\sin 3\theta$	Vertical trefoil
10	3	3	$\sqrt{8}\rho^3\cos 3\theta$	Oblique trefoil
11	4	0	$\sqrt{5}(6\rho^4-6\rho^2+1)$	Primary spherical aberration
12	4	2	$\sqrt{10}(4\rho^4-3\rho^2)\cos 2\theta$	Vertical secondary astigmatism
13	4	2	$\sqrt{10}(4\rho^4-3\rho^2)\sin 2\theta$	Oblique secondary astigmatism
14	4	4	$\sqrt{10}\rho^4\cos 4\theta$	Vertical quadrafoil
15	4	4	$\sqrt{10}\rho^4\sin 4\theta$	Oblique quadrafoil

Table 2.1: The Noll scheme first 15 terms of the real orthonormal Zernike circle polynomials in the polar coordinate and the values for n, m, and j.

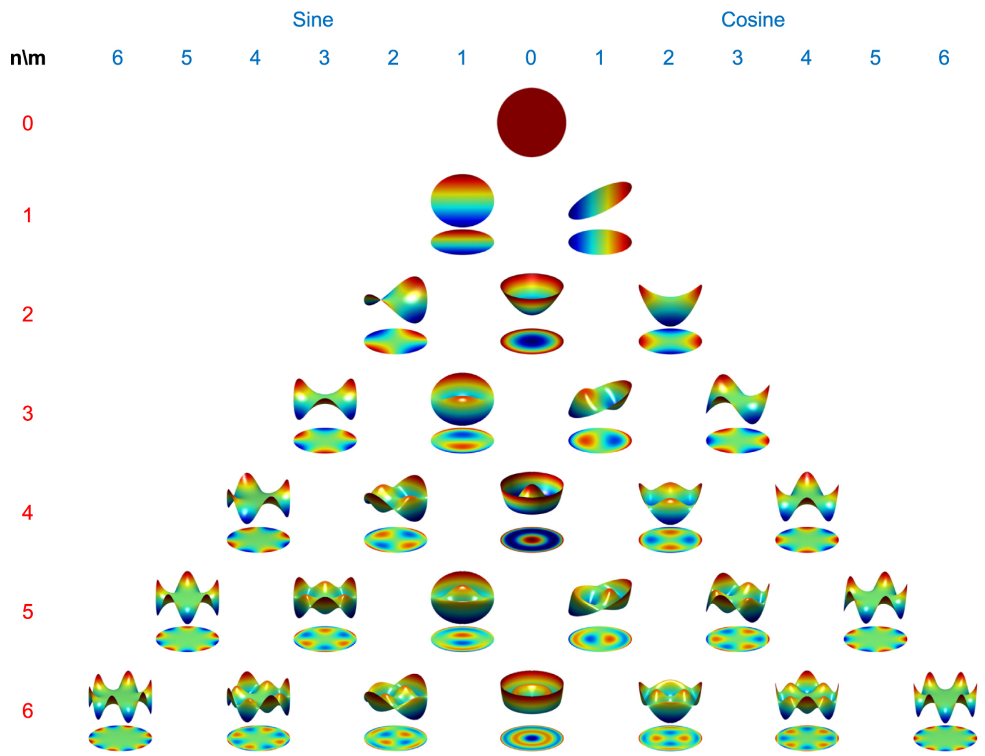

Figure 2.7: The pyramid of the non-normalized Zernike circle polynomials up to the sixth degree under the Noll indexing scheme, the figure is taken from [25].

Chapter 3

SLM and its calibrations

This chapter introduces a key component in the optical tweezer setup: the spatial light modulator (SLM). It begins by presenting the structure and working mechanism of the SLM, followed by a discussion of the various calibration techniques used, including phase calibration, Fourier calibration, and wavefront calibration. All calibrations were performed primarily using the Python package *slmsuite* [26].

3.1 Spatial light modulator

The spatial light modulator (SLM) enables modulation of the field phase of an incoming light beam. Figure 3.1 illustrates the basic structure of the SLM. The device consists of two layers of electrodes, with liquid crystal material positioned between them. The first layer electrode is a transparent conductive film located beneath the cover glass, which is maintained at a constant voltage. The second layer electrode consists of an array of reflective pixels, each of which can be individually addressed with analog voltage signals.

When a voltage difference is applied between the conductive film and a specific pixel, the liquid crystal molecules within the corresponding pixel are rotated by an angle related to the voltage difference. This rotation alters the refractive index of the liquid crystal for polarized light, particularly for light polarized along the slow axis of the SLM. Since each pixel can be controlled independently, different voltages can be applied across the pixel array, leading to a spatially varying refractive index profile.

When a collimated beam is directed onto the SLM screen, the reflected beam acquires a phase pattern corresponding to the refractive index variations at each pixel. In this way, the SLM enables phase modulation of the reflected light, making it an essential tool for controlling and shaping the optical tweezer array.

3.2 Pixelation of the SLM

As described in the previous section, the SLM consists of a large array of individual pixels. Due to this pixelated structure, the phase modulation achieved by the SLM is discrete rather than continuous. This section explores the effects of this pixelation on phase modulation and its impact on the optical system. A more detailed discussion of the implications of pixelation can be found in Ref. [28].

Consider an SLM with an array of $N \times M$ pixels, where the center-to-center spacing between pixels (the pitch) is denoted by p, and the width of each pixel is $w \leq p$. The

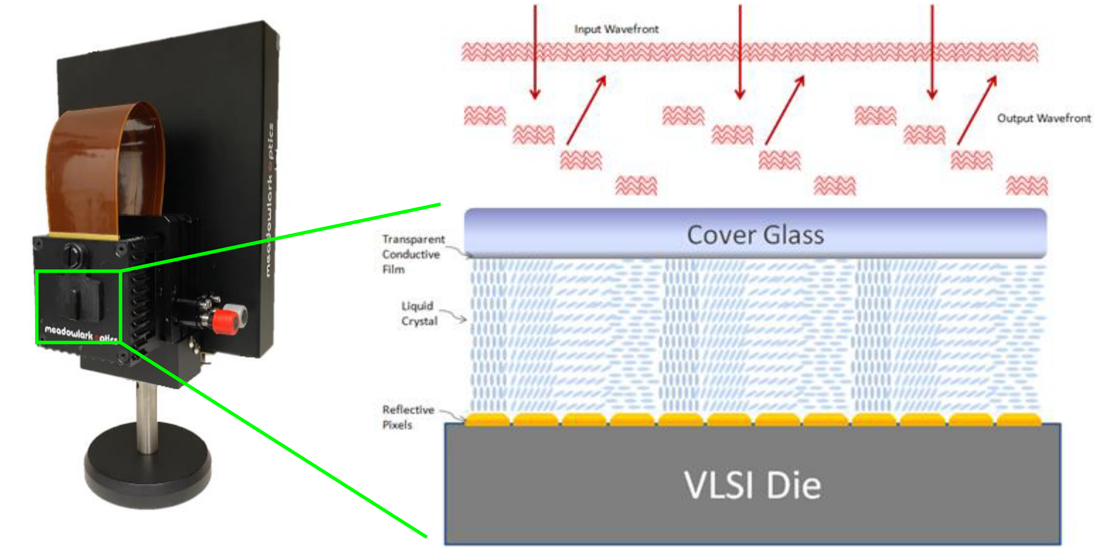

Figure 3.1: Cross-sectional illustration of a liquid crystal spatial light modulator, figure taken from [27]. The device consists of two layers of electrodes, with liquid crystal material positioned between them. The first layer is a transparent conductive film located beneath the cover glass, which is maintained at a constant voltage. The second layer consists of an array of reflective pixels, each of which can be individually addressed with analog voltage signals via the very large-scale integration semiconductor material (VLSI Die).

dimensions of the clear aperture of the SLM are therefore $W_1 = Np$ and $W_2 = Mp$.

When a continuous phase mask function $f(x, y) = \exp\{i\phi(x, y)\}$ is applied to the SLM, the actual phase modulation can be described as:

$$\tilde{f}(x,y) = \left(\text{rect}\left(\frac{x}{W_1}, \frac{y}{W_2}\right) \text{III}_p(x,y) f(x,y)\right) * \text{rect}\left(\frac{x}{w}, \frac{y}{w}\right), \tag{3.1}$$

where $\text{rect}(x, y)$ and $\text{III}(x, y)$ are rectangular and comb functions respectively, and $*$ represents convolution.

The field in the image plane is the Fourier transform of $\tilde{f}(x, y)$:

$$\begin{aligned}\tilde{F}(f_x, f_y) &= \frac{W_1 W_2 w^2}{p^2} \left\{\text{sinc}_\pi\left(W_1 f_x, W_2 f_y\right) * \text{III}_{\frac{1}{p}}(f_x, f_y) * F(f_x, f_y)\right\} \text{sinc}_\pi(w f_x, w f_y) \\ &= \frac{W_1 W_2 w^2}{p^2} \left\{\text{sinc}_\pi\left(W_1 f_x, W_2 f_y\right) * \sum_{n,m}^{\infty} F(f_x - \frac{n}{p}, f_y - \frac{m}{p})\right\} \text{sinc}_\pi(w f_x, w f_y),\end{aligned} \tag{3.2}$$

where $F(f_x, f_y)$ is the Fourier transform of $f(x, y)$. Notably, the SLM pixelation nature causes the field in the image plane $\tilde{F}(f_x, f_y)$ to be different from the Fourier transform of the programmed continuous phase $f(x, y)$. The interpretation of the result $\tilde{F}(f_x, f_y)$ can be decomposed into the following steps:

1. Inside the curly bracket there is summation for $F(f_x - \frac{n}{p}, f_y - \frac{m}{p})$, where each term is a translated version of the original Fourier transform result $F(f_x, f_y)$.

2. Each term within the summation is convoluted with the $\mathrm{sinc}_\pi(W_1 f_x, W_2 f_y)$ function, which causes a broadening.

3. The amplitude of the term inside the curly bracket is modulated by an envelope function $\mathrm{sinc}_\pi(w f_x, w f_y)$. Its width is much broader than the width of $\mathrm{sinc}_\pi(W_1 f_x, W_2 f_y)$ given that $w \ll W_1, W_2$.

Furthermore, this factor $\frac{W_1 W_2 w^2}{p^2}$ indicates that a higher filling ratio w/p leads to increased intensity for the modulated image.

To better understand Eq. 3.2, consider a blaze grating phase $\phi(x, y)$ with spatial frequencies (f_{x0}, f_{y0}) programmed on the SLM,

$$\phi(x, y) = f_{x0} \cdot x + f_{y0} \cdot y + \phi_0, \tag{3.3}$$

where ϕ_0 is an arbitrary constant phase. The Fourier transform of $f = \exp\{i\phi(x, y)\}$ is a delta function:

$$F(f_x, f_y) = \delta(f_x - f_{x0}, f_y - f_{y0}). \tag{3.4}$$

The summation in the curly bracket of Eq. 3.2 becomes another Dirac comb:

$$\sum_{n,m}^{\infty} F(f_x - \frac{n}{p}, f_y - \frac{m}{p}) = \sum_{n,m}^{\infty} \delta(f_x - f_{x0} - \frac{n}{p}, f_y - f_{y0} - \frac{m}{p}) = \mathrm{III}_{\frac{1}{p}}(f_x - f_{x0}, f_y - f_{y0}), \tag{3.5}$$

which translates $\mathrm{sinc}_\pi\,(W_1 f_x, W_2 f_y)$ by different amounts, and the result is modulated by the sinc envelope $\mathrm{sinc}_\pi(w f_x, w f_y)$. The Eq. 3.2 simplifies to:

$$\tilde{F}(f_x, f_y) = \frac{W_1 W_2 w^2}{p^2} \sum_{n,m}^{\infty} \mathrm{sinc}_\pi(W_1(f_x - f_{x0} - \frac{n}{p}), W_2(f_y - f_{y0} - \frac{m}{p}))\mathrm{sinc}_\pi(w f_x, w f_y). \tag{3.6}$$

For the SLM (Meadowlark E19x12) we use in our experiment, the relevant parameters are $W_1 = 15.36$ mm, $W_2 = 9.6$ mm, $w = 8$ μm, $p = 7.82$ μm [29]. For simplicity, only the y-dimension is considered. The main lobe width of the sinc function $\mathrm{sinc}_\pi(W_2(f_y - f_{y0} - \frac{m}{p}))$ is $2/W_2 \approx 208.4$ m^{-1}, while the period of the comb function $\mathrm{III}_{\frac{1}{p}}$ is $1/p \approx 1.28 \times 10^5$ m^{-1}, and the main lobe width of the envelope $\mathrm{sinc}_\pi(w f_x, w f_y)$ is $2/w \approx 2.5 \times 10^5$ m^{-1}. Numerical results show that the main lobe width of $\mathrm{sinc}_\pi(W_2(f_y - f_{y0} - \frac{m}{p}))$ is significantly smaller than both the comb spacing of $\mathrm{III}_{\frac{1}{p}}$ and the width of envelope $\mathrm{sinc}_\pi(w f_x, w f_y)$.

Fig. 3.2 (a) illustrates the result of Eq. 3.6 when $f_{y0} = 3 \times 10^5\ \mathrm{m}^{-1}$. The red curve represents the envelope $\mathrm{sinc}_\pi(wf_x, wf_y)$, and the blue curve shows the overall result. The multiple peaks of the blue curve are modulated by the envelope. Fig. 3.2 (b,c) provide a zoomed-in view of the first two peaks within the envelope's main lobe, which correspond to the ± 1 orders of the blaze grating.

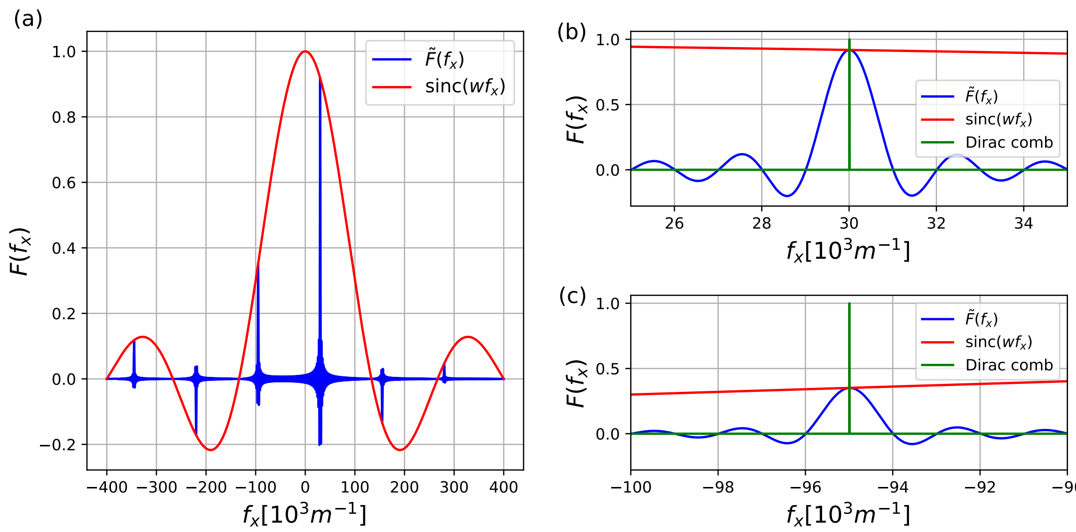

Figure 3.2: Image plane results for a blaze grating phase. (a) illustrates the result of Eq. 3.6. The red curve represents the envelope $\mathrm{sinc}_\pi(wf_x, wf_y)$, and the blue curve is the overall result, which has multiple peaks and its amplitude is modulated by the envelope. (b,c) show the zoomed-in view of the first two peaks within the main lobe of the envelope, they are denoted as the ± 1 order of the blaze grating.

According to discrete Fourier theory, the highest spatial frequencies in Fourier space are constrained by the inverse of the pixel width in real space, meaning the blaze spatial frequencies $f_{x0}, f_{y0} \leq 1/w$. This ensures that the $+1$ order $f_x = f_{x0}, f_y = f_{y0}$ always lies within the main lobe of the sinc envelope, guaranteeing maximal intensity is taken at the $+1$ order. In addition to the ± 1 order, higher-order peaks appear outside the main lobe, consistent with experimental observations of multiple spots at long camera exposure times.

3.3 Phase calibration

The phase modulation of the SLM is achieved by controlling the refractive index of the liquid crystal through voltage applied to each individual pixel. The mapping between voltage and phase is not fixed and requires recalibration whenever the wavelength of the light changes or the SLM is reinstalled on the breadboard. This is because the refractive index of the liquid crystal medium varies with wavelength, and the reinstallation can slightly change the incident angle of the beam, which consequently alters the optical path length through the liquid crystal.

This section only provides a brief overview of the phase calibration procedure. A more detailed discussion can be found in Ref. [17].

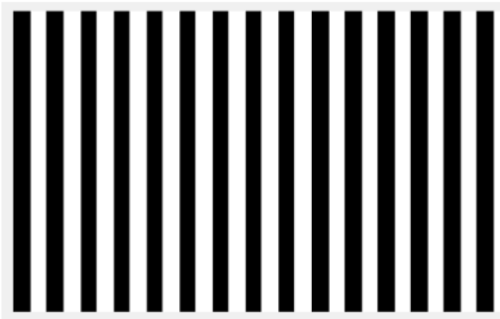

Figure 3.3: Binary strip voltage pattern applied to the SLM.

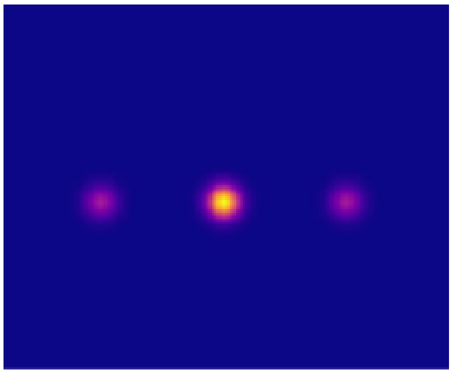

Figure 3.4: Diffraction pattern recorded by the camera.

The calibration procedure involves the following steps:

1 **Linear voltage scan**: A binary strip voltage pattern, as shown in Fig. 3.3, is applied to the SLM. As suggested by the Meadowlark SLM manual [27], the width of each strip is typically chosen to be 4 or 8 physical pixels. The voltage of the white strips is set to the maximum voltage (5V), whilst the black strips' voltage is linearly varied from 5V to 0V. For each of the scanned voltage, there is a camera measuring diffraction orders produced by this binary phase pattern. Fig. 3.4 shows the diffraction pattern where the 0th diffraction order appears at the center, while the ± 1 orders are located to the left and right. The phase difference between the black and white strips is determined from the observed intensities:

$$I_0 = \frac{1}{2}(1 + \cos \Delta\phi) \tag{3.7}$$

$$I_{\pm 1} = \frac{1}{\pi}(1 - \cos \Delta\phi) \tag{3.8}$$

where $\Delta\phi$ is the phase difference, and it depends on the voltage difference ΔU between the black and white strips, i.e., $\Delta\phi = \Delta\phi(\Delta U)$. I_0 and $I_{\pm 1}$ represent the intensities of 0 and ± 1 diffraction order. The intensity values are integrated over the regions corresponding to each diffraction order for every voltage step in the scan.

2 **Phase unwrapping**: Meadowlark Optics provides a Look-Up Table (LUT) generator to determine the mapping from the voltage difference ΔU to the phase difference $\Delta\phi$. By inputting a .csv file where one column contains the intensity values of the 0th or ± 1 orders, and another column contains integer values from

255 to 0 corresponding to the linear voltage scan index, a LUT can be generated. In our experiment, the average intensity of the ± 1 orders was used as the input for the 1st-order intensity.

3.4 Fourier calibration

When generating a tweezer array, it is often more intuitive to specify the positions of tweezers in the frame of the camera rather than the Fourier space of the SLM. Therefore, determining the mapping between the SLM's Fourier space and the camera's real space is important. According to Eq. 2.9, the mapping is given by the relation $(f_x, f_y) = (\frac{M^2 x}{\lambda f}, \frac{M^2 y}{\lambda f})$. However, this is only true in the ideal alignment scenario where the optical axis passes perpendicularly through the center of the camera, and the latter is positioned exactly at the focal plane of the Fourier lens. In practical experiments, due to the displacement, tilt, and out-of-focus of the camera, the mapping is different from the ideal case and needs to be recalibrated whenever modifications are made to the optical systems.

The slmsuite package provides all the necessary tools for implementing this calibration in imperfect alignment settings, which is referred to as the Fourier calibration. Detailed information about the package can be found in Ref. [26]. The essential concept behind this calibration is assuming that any vector $\vec{k}$ in SLM's Fourier space and its associated vector $\vec{x}$ in the real space of the camera can be related by:

$$\vec{x} = M \cdot (\vec{k} - \vec{a}) + \vec{b}, \tag{3.9}$$

where M is a 2x2 transformation matrix, and $\vec{a}$ and $\vec{b}$ are 2x1 vectors representing the offset. The calibration is achieved by generating an array in the Fourier space of the SLM, with two missing points in one of its corners to indicate the orientation of the array when observed by the camera, see Fig. 3.5. By processing the image of this array, the calibration function can determine the value of M, $\vec{a}$, and $\vec{b}$.

3.5 Wavefront calibration

In an ideal optical system, optimal imaging performance requires the constructive interference of all light rays passing through the system. However, the presence of aberrations introduces phase shifts in different regions of the wavefront, distorting it and causing destructive interference, which reduces the image brightness and clarity.

There are multiple sources of aberrations in the optical tweezer setup. The first source is the inherent limitations in the fabrication process of SLMs, such as backplane curvature and variations in the thickness of the liquid crystal layer across the aperture. The second source is the imperfections of optical components and the misalignment. However, one of the key advantages of using an SLM is the ability to correct the aberrations by imprinting a correction phase on it. Several traditional wavefront calibration methods exist for

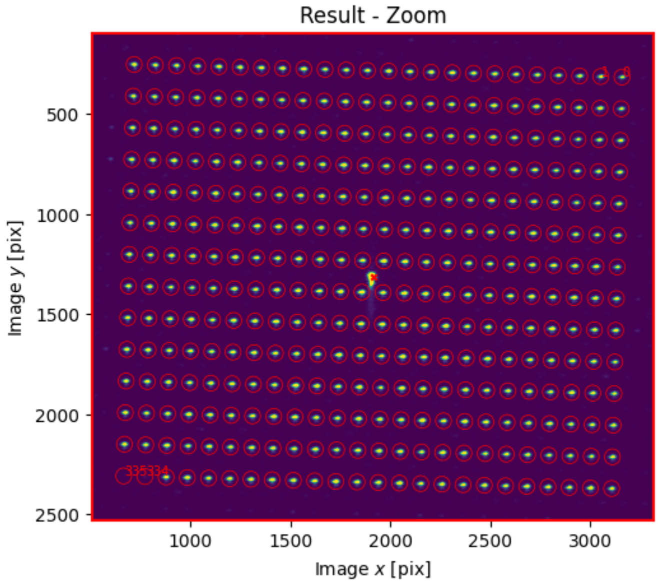

Figure 3.5: Fourier calibration array observed in the camera. There are two missing points in the lower left corner to indicate the orientation of the array.

determining the correction phase, such as interferometry [30], Shack-Hartmann wavefront sensors [31], and phase retrieval techniques [32].

In the experiment, we utilized the *slmsuite* package [26] to perform the wavefront calibration (WFC). The package offers two calibration methods: one based on the interference of subregions of the SLM, known as the superpixel method, as proposed in Ref. [33], and the other one is by scanning Zernike polynomial coefficients to optimize the spot size observed on the camera. We primarily employed the first method, as the second method is not yet fully developed.

3.5.1 Superpixel interference method

The superpixel interference method measures the phase differences between subregions of the wavefront using interference patterns. Once the phase is obtained for each subregion, interpolation is applied to smooth any artifacts caused by pixelation.

The method involves the following steps:

- **Step 1: Setup Configuration**. The SLM is positioned in front of a Fourier lens, and a CCD camera is placed at its focal plane to serve as the Fourier plane.
- **Step 2: Superpixel Division**. The SLM screen is divided into equal rectangular subregions, each composed of several physical pixels. These subregions, referred to as "superpixels," are the fundamental units for the interference calibration.
- **Step 3: Interference with a Reference Superpixel**. One superpixel, typically at the center of the SLM aperture, is chosen as the reference. The phase difference

between the reference superpixel and the probed superpixel is measured using interference: A blazed grating phase is applied to both the reference and the probed superpixel such that the lights reflected by them reach the same point on the camera, which gives rise to the interference. The remaining superpixels are directed out of the camera's frame by applying a large blaze angle to eliminate their influence. Figure 3.6(a) shows an example of the blazed grating applied to the SLM, with (b),(c) the interference pattern observed at the camera. The probed superpixel is at position (500,500) in the SLM aperture, and the reference is at the center.

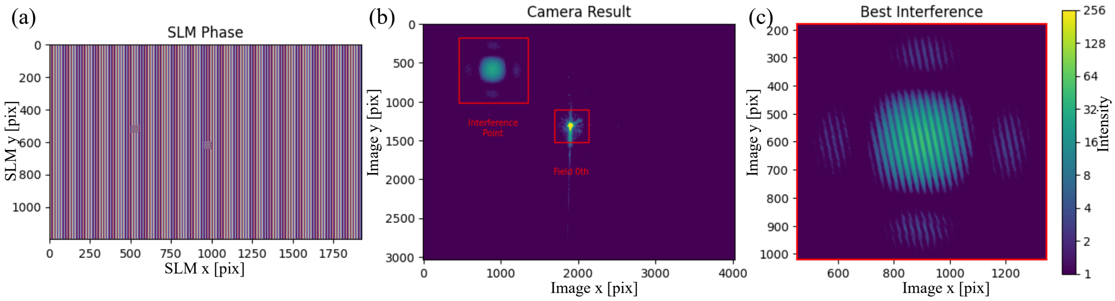

Figure 3.6: Superpixel interference method. (a) A blazed grating phase is applied to both the reference and the probed superpixels, steering their light to the same point on the camera to generate interference. The remaining superpixels are directed out of the camera's frame by applying a large blaze angle to eliminate their influence. (b) The interference pattern observed by the camera, note there is also the 0th spot in the center. (c) A zoom-in figure of the interference fringes.

- **Step 4: Interference Intensity**. The intensity in the center (x_0, y_0) of the interference pattern follows the relation

$$I(x_0, y_0) = |E_1|^2 + |E_2|^2 + 2|E_1||E_2| \cos(\phi_1 - \phi_2), \tag{3.10}$$

where $E_1 = |E_1| \exp\{i\phi_1\}$, $E_2 = |E_2| \exp\{i\phi_2\}$ represent the fields on the probed and reference superpixels respectively.

- **Step 5: Phase Scanning**. A constant phase ϕ_s is added to the blazed phase of the probed superpixel, modifying Eq. 3.10 to:

$$I(x_0, y_0) = |E_1|^2 + |E_2|^2 + 2|E_1||E_2| \cos(\phi_1 + \phi_s - \phi_2). \tag{3.11}$$

By scanning ϕ_s in the range $[0, 2\pi]$, a sinusoidal signal is yielded, see Fig. 3.7. The maximum and minimum intensities correspond to $(|E_1|+|E_2|)^2$ and $(|E_1|-|E_2|)^2$, from which the field amplitudes on both superpixels can be extracted. The phase difference between the probed and reference superpixels is determined by the value of ϕ_s at the maximum intensity of $I(x_0, y_0)$, where $\phi_s = \phi_2 - \phi_1$. A R^2 value is also calculated to assess the fit of the sinusoidal signal, with lower R^2 values indicating superpixels that are not illuminated.

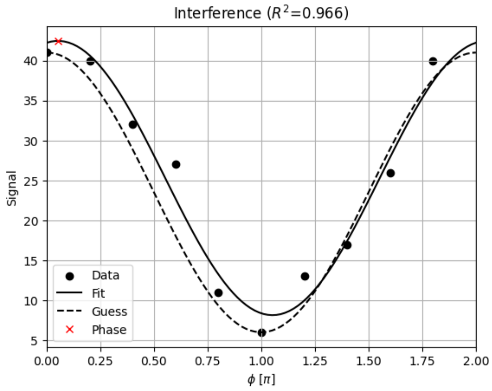

Figure 3.7: Phase scanning of probed superpixel. The phase difference between the probed and reference superpixels is determined by the value of ϕ_s at the maximum intensity (red cross in the figure), where $\phi_s = \phi_2 - \phi_1$.

- **Step 6: Superpixel Iteration**. The described procedure is repeated for each superpixel, generating a pixelated phase image of the wavefront. Superpixels with low R^2 values are discarded, and the resulting phase image is smoothed using a Gaussian kernel to eliminate discontinuities between superpixels. The Fig. 3.8 shows the result of the WFC calibration. (a) is the correction phase image after the smoothing, (b) illustrates the measured amplitude on the SLM screen, and (c) represents the fitting assessment value R^2 for each superpixel.

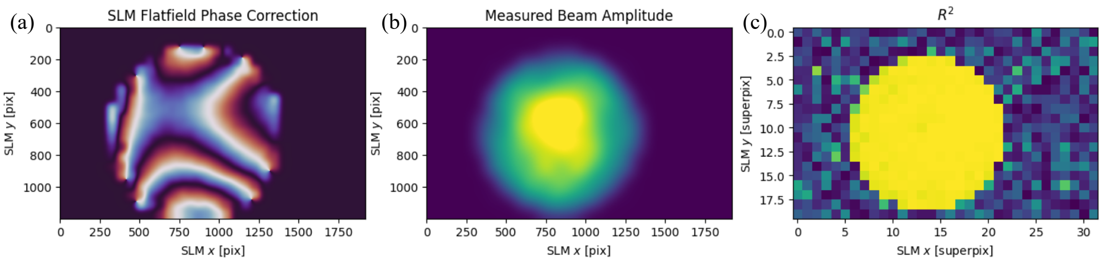

Figure 3.8: Wavefront calibration result: (a) Smoothed aberration phase mask, (b) measured light intensity on the SLM aperture, (c) 2D plot of the fitting accuracy R^2.

Assumption and Validation

The assumption that the phase is constant across each superpixel is valid if the aberration variation across the aperture is slow. This is confirmed by the interference pattern shown in Fig. 3.6(c). The interference fringes show a sinc envelope, which is caused by the square-shaped aperture of the superpixel. These fringes are generated as the beams originating from the probed and reference superpixel are striking on the interference point at different angles θ_1, θ_2, resulting in different projections of wave vector $\vec{k_1}(\theta_1), \vec{k_2}(\theta_2)$ on the x-y (camera) plane. The spatial frequency of the fringes follows the difference $\vec{k_1}(\theta_1) - \vec{k_2}(\theta_2)$. If a significant variation of aberration exists within a superpixel, it would cause noticeable distortion to the interference fringes. However, in practical experimental conditions, no such distortion has been observed, validating the assumption of slow phase variation across each superpixel.

3.5.2 Zernike coefficients scan method

The *slmsuite* package is also developing a wavefront calibration method based on scanning Zernike coefficients. This method leverages the orthogonality of Zernike polynomials by iteratively adjusting and subtracting Zernike coefficients to minimize a predefined merit function, which is typically the spot size observed in the camera. One of the key advantages of this approach is its reduced time consumption compared to the superpixel interference method, which requires a phase scan for each individual superpixel.

This method has not been tested in our experiment due to the challenges posed by the small tweezer waist (approximately 1.2 μm), which makes it difficult for the merit function to reliably measure the spot size. However, the slmsuite documentation reports the successful implementation of the Zernike coefficient scan up to the Z_9 coefficient, achieving good convergence with coefficient stability better than 0.2 radians.

Chapter 4

Experimental setup

This chapter introduces the experimental setup of the optical tweezer experiment. The main challenge to address is the limited optical access to the existing vacuum chamber. In particular, the tweezer light, the MOT light, and the collected atomic fluorescence need to be combined through the same viewport. This challenge can be overcome with a small modification of the existing MOT design, by using an optical mirror with a hole. The following discussion presents the design of the mirror and the description of the optical setup.

4.1 Setup design

Fig. 4.1 shows a schematic illustration of the optical tweezer setup. The tweezer light (532 nm) is represented in green, and the MOT light (423 nm) is depicted in purple. On the lower portion of the figure, there is a rectangular mirror with a hole in the center, positioned at a 45° angle where the tweezer and MOT beams cross. The mirror's front surface is coated to reflect the tweezer light, while the rear surface is polished intentionally to collect part of the light for diagnostic purposes. A 1 mm diameter hole, created at a 45° angle to the front surface (see Figures 4.2 and 4.3), allows the MOT light to pass through. The mirror's special design serves multiple purposes:

- **Redirecting the tweezer light**: The tweezer light enters from the left and gets reflected by the mirror. Most of the light, except the portion shining on the hole, is redirected to the tweezer lens (f_6), which focuses it into the vacuum chamber (the enclosed region in Fig. 4.1).

- **Allowing MOT Light to Pass**: The MOT light, initially traveling downwards, is focused by a plano-convex lens (f_5). The geometric center of the hole coincides with the focal point of the lens, allowing the converging MOT light to pass through the mirror. The light is then collimated by the tweezer lens (f_6) and directed into the vacuum chamber through the viewport glass. On the opposite side of the vacuum chamber, there is a $\lambda/4$ plate for 423 nm flipping the polarization of the MOT beam from σ^+ to σ^-. The light then encounters a bandpass filter, which reflects the MOT beam while allowing the tweezer beam to go through.

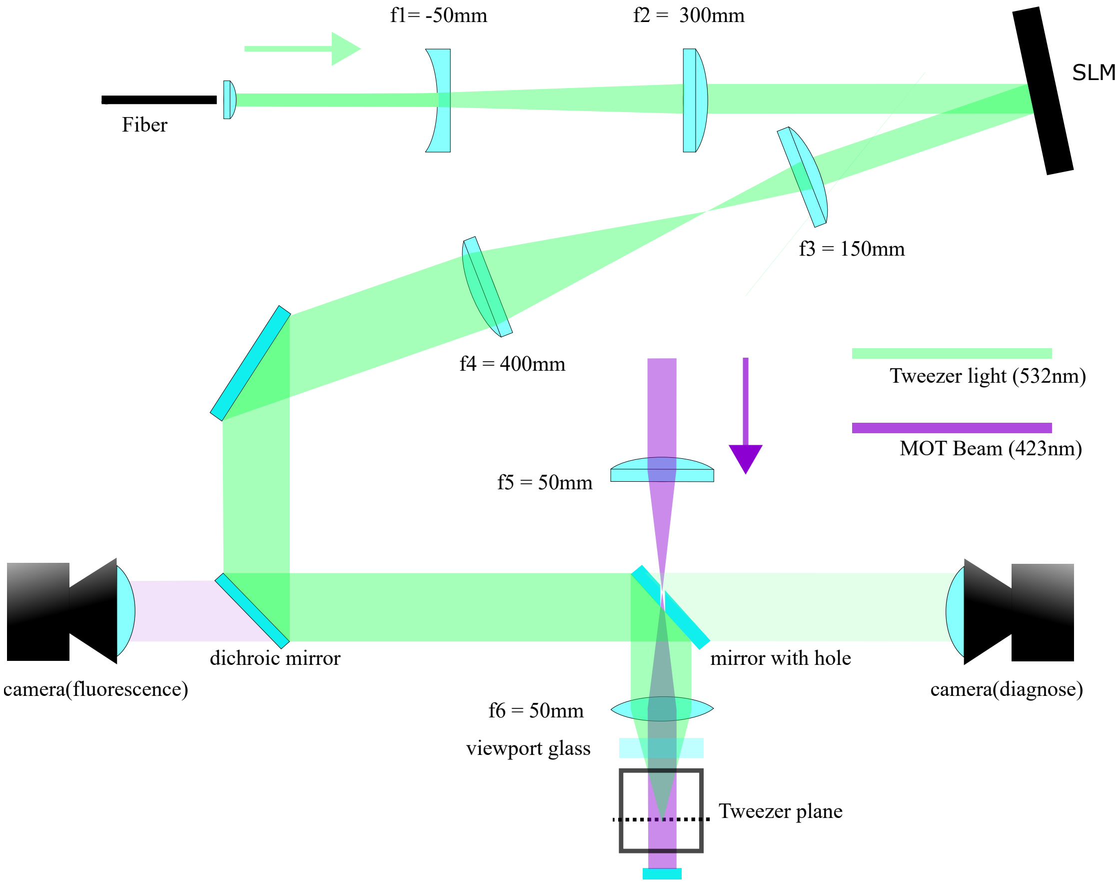

Figure 4.1: The illustration of the optical tweezer setup: The tweezer light first passes through an aspherical lens for collimation. A Galilean telescope (f_1 and f_2) expands the beam to illuminate as many SLM pixels as possible while maintaining about 99% of the beam's power within the SLM screen, ensuring higher resolution of phase modulation and avoiding light cropping. Following the SLM, another Keplerian telescope (f_3 and f_4) further expands the beam, achieving a theoretical tweezer waist of around 1 μm) inside the vacuum chamber. The SLM-to-f_3 lens distance equals the effective focal length of f_3 (150 mm), while the tweezer lens-to-f_4 distance matches the focal length of f_4 (400 mm). This configuration ensures the chief rays from the diffracted beams all pass through the center of the tweezer lens. A mirror with a hole reflects the tweezer light toward the tweezer lens f_6, which focuses it into the vacuum chamber to form the tweezer array. The MOT light passes through the mirror hole, converged by lens f_5 and collimated by f_6 into the vacuum chamber (enclosed by the square). Two cameras are positioned on opposite sides: one collects atom fluorescence, while the other diagnoses the tweezer array.

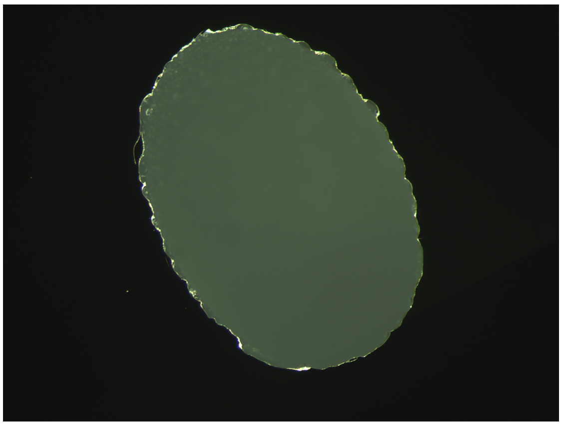

Figure 4.2: Microscope image of the mirror's hole, which has a diameter of 1 mm and a 45° tilt with respect to the front surface of the mirror, giving it an elliptical appearance in the image.

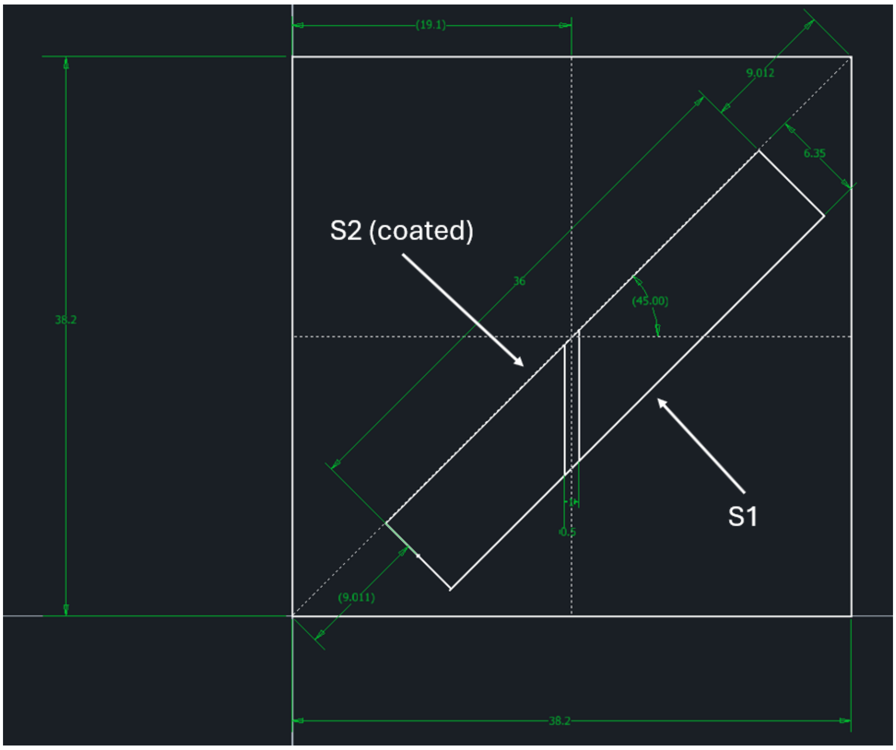

Figure 4.3: Design of the mirror with a hole made by Silvan Koch. The front and rear surfaces measure 36 mm × 25 mm, with a thickness of 6.35 mm. A 1 mm-diameter hole passes through the center of the front surface S_2 at a 45 ° angle. The surface S_2 is coated to reflect both tweezer light (532 nm) and atom fluorescence (423 nm), while the rear surface S_1 is polished to allow a small portion of the tweezer light to pass through.

- **Separating Fluorescence from the MOT Light**: The fluorescence emitted by the atoms in the vacuum chamber is collimated by the tweezer lens and reflected by the mirror with a hole. Simultaneously, the MOT light is converged by the tweezer lens and passes through the mirror. This configuration ensures that the reflected MOT light does not mix with the fluorescence, thereby improving the reliability of atom detection.

Now, let's move to the top part of the figure, which corresponds to the path of the tweezer light. The tweezer light, emerging from the fiber collimator, initially has a waist of approximately 500 μm. Before it reaches the mirror with a hole, it travels through several optical components:

- **Galilean telescope**: After the fiber collimator, a Galilean telescope is used to magnify the beam. In this setup, we use lenses with focal lengths $f_1 = -50$ mm and $f_2 = 300$ mm to achieve a magnification factor of $m = 6$, resulting in an output beam waist of approximately 3 mm. This allows the tweezer light to have a larger waist, enabling it to illuminate more pixels on the SLM. The larger illumination area improves the phase modulation resolution of the SLM. At the same time, it ensures that approximately 99% of the beam's power remains within the SLM screen, preventing light cropping, which would reduce the effective NA of the set-up.

- **SLM aperture**: The SLM is positioned such that the tweezer beam illuminates the center of its clear aperture. To optimize phase modulation performance, the incident angle of the beam on the SLM is kept small (around 10°). After phase modulation, the SLM reflects the beam into a Keplerian telescope for further manipulation.

- **Keplerian telescope**: The Keplerian telescope, consisting of two convex lenses with focal lengths ($f_3 = 150$ mm) and ($f_4 = 400$ mm), provides a magnification factor $m \approx 2.67$. This magnification factor is chosen to further increase the beam waist such that a small theoretic tweezer waist value around 1 μm is obtained inside the vacuum chamber. For the same reason discussed before, the magnification should not be made too large, as approximately 99% of the power must still be enclosed within the clear aperture of the tweezer lens.

  The distance from the SLM to the first lens of the Keplerian telescope must be equal to the effective focal length of the lens ($f_3 = 150$ mm), and the distance from the tweezer lens to the second lens of the telescope should match the focal length of the second lens ($f_4 = 400$ mm). This configuration ensures that the chief rays of the diffracted beams after the SLM all pass through the center of the tweezer lens, as illustrated in Fig. 4.4. If this arrangement is not satisfied, the chief ray of each diffracted beam would strike different areas of the tweezer lens, leading to different aberrations or more seriously causing light cropping. Therefore, the Keplerian configuration is essential for preventing such issues.

In the experimental setup, two imaging paths are incorporated to enable real-time monitoring of the process. The first path is designed for imaging atoms through their

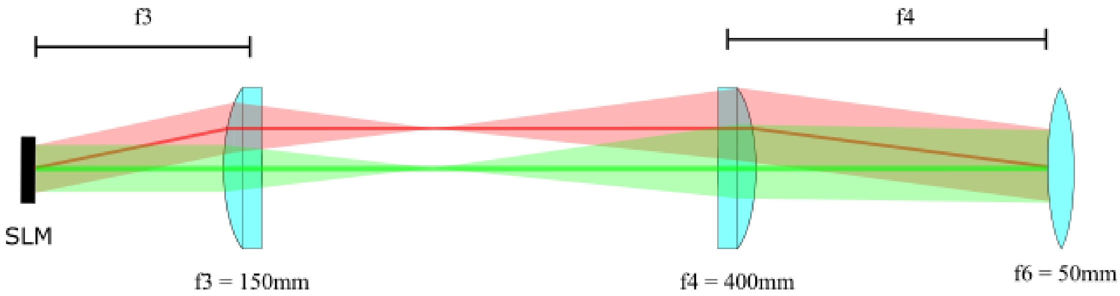

Figure 4.4: The special arrangement of the Keplerian telescope. The distance from the SLM to the first lens of the Keplerian telescope must be equal to the effective focal length of the lens ($f_3 = 150$ mm), and the distance from the tweezer lens to the second lens of the telescope should match the focal length of the second lens ($f_4 = 400$ mm). This configuration ensures that the chief rays of the diffracted beams after the SLM all pass through the center of the tweezer lens, minimizing aberrations and preventing light cropping.

fluorescence, while the second path is dedicated to inspecting the tweezer array. Two CCD cameras are employed, referred to as the fluorescence camera and the diagnostic camera, each serving distinct functions.

- **Fluorescence path**: The fluorescence camera, positioned on the left side of Fig. 4.1, captures atom fluorescence, which indicates the presence of atoms within the trap. As the atoms fluoresce, the light is collimated by the tweezer lens and reflected by the mirror with a hole. The reflected fluorescence then passes through a dichroic mirror and is captured by the camera.

  There are two possible choices for this dichroic mirror. The first option is to use a dichroic mirror that reflects the tweezer light and transmits the fluorescence as shown in Fig. 4.1. However, the commercially available dichroic mirrors (e.g., from Thorlabs) are typically very thin (1 mm), which can result in surface bending when mounted, introducing substantial aberrations. To mitigate this, custom dichroic mirrors with a larger thickness were ordered. Due to the long leadtime, for the initial setup, a Thorlabs dichroic mirror that transmits the tweezer light while reflecting the fluorescence was used.

- **Diagnostic path**: The second camera, located on the right side of Fig. 4.1, monitors the tweezer array. After merging the tweezer setup with the vacuum apparatus, it is no longer possible to place a camera at the focal plane of the tweezer lens to observe the array directly. Hence, a diagnostic camera becomes important for debugging and monitoring the tweezer status. To get the diagnostic light, the rear surface of the mirror with a hole is intentionally polished. This allows a small portion of the tweezer light to pass through the mirror and be captured by the diagnostic camera.

Similar to the tweezer light, the distance from the lens of the diagnostic camera (not shown in the figure) to the second lens of the telescope should also equal to f_4 to ensure that the chief rays pass through the center of the lens. Notably, the tweezer light and the diagnostic light follow the same optical path up to the mirror with a hole, making it interesting to explore the correlation between the results of wavefront calibration effectuated by a camera positioned at the tweezer lens focus and by the diagnostic camera.

4.2 Setup in real experiment

The tweezer setup is built and tested on a separate breadboard using standard Thorlabs components. At this stage, all tests and characterizations are conducted exclusively on the breadboard. Once these tests are completed, the breadboard will be installed in the main experiment. A few cut-outs of the breadboard have been made to accommodate existing components in the vacuum apparatus such as the effusive oven used to generate the atomic beam and the vacuum pump.

Fig. 4.5 presents the top and side views of the experimental setup. In the top view, the tweezer light first passes through a "U"-shaped Galilean telescope constructed using Thorlabs' cage system. The "U" shape begins with an XY translation mount, which holds the output of a high-power optical fiber (part no. LMA-PM-15) from NKT Photonics. At the end of the "U"-shaped path, a half-wave plate and a PBS (polarizing beam splitter) are used to adjust and purify the beam's polarization. This ensures the polarization is aligned with the slow axis of the SLM, which is critical for effective phase modulation. After being modulated by the liquid crystal screen of the SLM, the tweezer light is then reflected into a "U"-shaped Keplerian telescope. To optimize the SLM's performance, the incident and reflected light should make an angle of approximately 15 degrees.

As mentioned earlier, two options exist for the dichroic mirror to separate the atom fluorescence. For the initial tests, a dichroic mirror that transmits the tweezer light is mounted on a cage cube located just after the Keplerian telescope (though this cube is not depicted in the figure).

A periscope is placed after the dichroic mirror cage cube to direct the beam downward. The right side of Fig. 4.5 shows the side view of the setup. The periscope directs the tweezer light onto the mirror with a hole, which is mounted in a cage cube. Most part of the light is reflected by the mirror, while a small portion passes through the mirror for diagnostic purposes. The MOT light input is located just above the mirror with a hole. A convex lens converges the MOT light, allowing it to pass through the hole in the mirror. Below the mirror, the tweezer lens focuses the tweezer light into the vacuum chamber while simultaneously collimating the MOT beam.

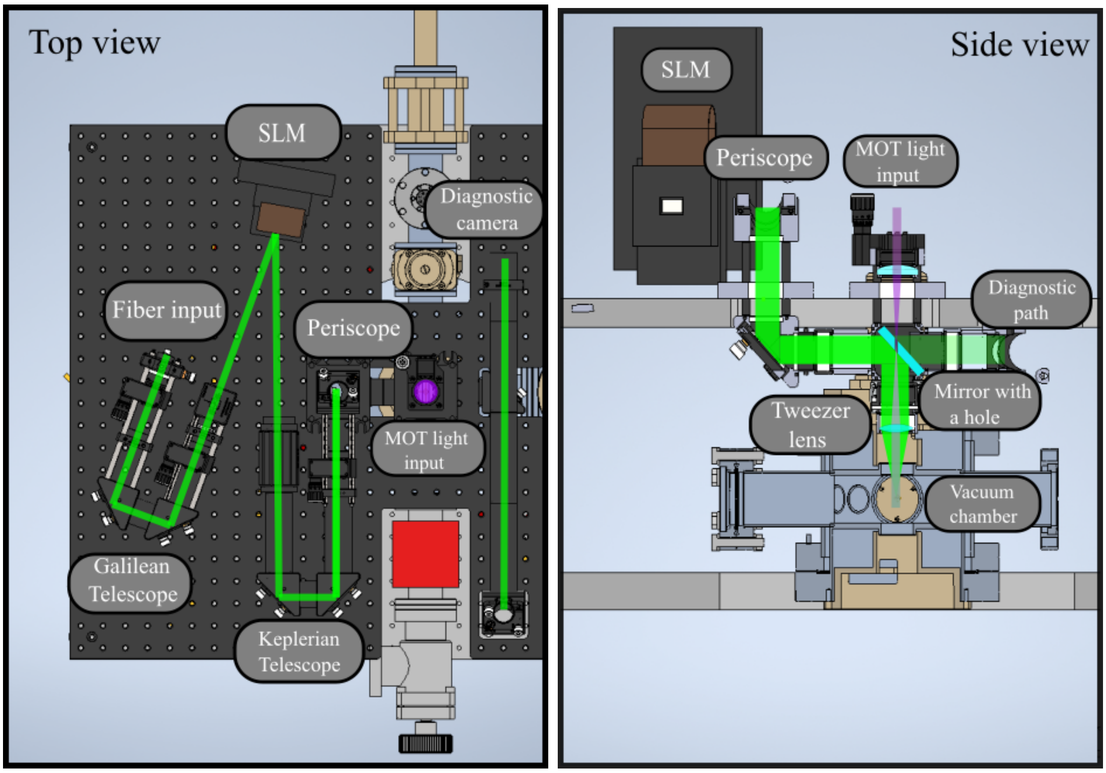

Figure 4.5: Top and side view of the experimental setup. **Top view**: The tweezer light first passes through a "U"-shaped Galilean telescope. The "U" shape begins with an XY translation mount connected to the output of an optical fiber. After the fiber mount, a fiber collimator is mounted on a Z translation mount. Once collimated, the tweezer beam enters the telescope, where the first lens is mounted on a cage plate and the second lens is on a Z translation mount. Two mirrors between the lenses are used to redirect the beam. At the end of the "U" shape, a half-wave plate and a polarizing beam splitter (PBS) adjust and purify the polarization of the beam, aligning it with the slow axis of the SLM for optimal modulation. After passing through the SLM, the modulated tweezer light is reflected into a "U"-shaped Keplerian telescope. In this telescope, the first lens is mounted on an adjustable lens tube, and the second lens is on a Z translation mount. Two additional mirrors steer the beam between the lenses. A periscope directs the light downward. **Side view**: the periscope guides the tweezer light onto the mirror with a hole. Most of the light is reflected by the mirror with a hole, while a small portion of the light goes in the transmission of the mirror to the diagnostic path. The MOT light input is located above the mirror, and a convex lens mounted on a Z translation mirror mount focuses the MOT light so that it passes through the hole in the mirror. Below the mirror, the tweezer lens converges the tweezer light into the vacuum chamber while collimating the MOT beam.

For completeness, the specifications of the key devices and optics used in the setup are listed below:

Item	Manufacturer	Part number	Resolution	Pixel pitch
SLM	Meadowlark	E19x12	1920x1200	8.0x8.0 μm
Cameras	Allied Vision	1800 u-1240m	4024x3036	1.85x1.8 μm

Table 4.1: Specification for the main devices used in the optical tweezer setup.

Item	Manufacturer	Part number	Material
All telescope lenses	Lens optics	Customized	Fused silica
Mirror with hole	LAYERTEC	Customized	Fused silica
Dichroic mirror(test)	Thorlabs	DMLP490R	Fused silica
Tweezer lens	Asphericon	AFL25-50-U	Fused silica
MOT light input lens	Thorlabs	LA1255-A	N-BK7
Diagnostic camera lens	Thorlabs	LA1978-AB	N-BK7

Table 4.2: Specification for the essential optics used in the optical tweezer setup.

Chapter 5

Setup characterizations and tests

This chapter focuses on the characterization of the optical tweezer setup. The first section introduces two methods for measuring the waists of the individual Gaussian beams that constitute the tweezer array. Following that, the section presents how specific components influence the tweezer waist. The second section demonstrates two techniques for shifting the location of the tweezer focal plane. The third section investigates the correlation between the aberration correction phases obtained from the tweezer camera and the diagnostic camera. The last section presents the Zernike coefficient decomposition of the essential optics' interferometry image to study their aberrations.

5.1 Tweezer's beam waist

The waist of each Gaussian beam in an optical tweezer array is a critical parameter, as it directly affects the trapping potential. This section presents two methods for measuring the waist of individual tweezers: the second-moment method and the knife-edge measurement method. Additionally, it discusses how various optical components—such as the dichroic mirror for atom fluorescence, the mirror with a hole, the viewport glass, and the presence of ring electrodes within the vacuum chamber—impact the tweezer waist.

5.1.1 Waist measurement methods

According to the calculation, the theoretical value for the waist of the tweezer is approximately 1 μm. This value is derived by multiplying the initial beam waist from the fiber collimator by the magnification factors of the telescopes and applying the lens waist transformation formula. On the other hand, the pixel size of the camera is 1.8 μm, which is larger than the waist of the tweezer. For this reason, it is difficult to measure the tweezer waist by some direct methods like the 2D Gaussian fitting.

There are two ways to mitigate this problem. The first is to use a microscope tube, which consists of an objective lens and an eyepiece mounted on the same lens tube, providing a total magnification of 22.2$\times$. By positioning the microscope objective near the tweezer plane and inserting the camera at the output of the microscope tube, the tweezer array image is magnified before being captured by the camera, as shown in Fig. 5.1. After magnification, the spot size becomes significantly larger than the camera's pixel size, making common methods like Gaussian fitting or second-moment calculations feasible again. The downside of this method is that the lens of the microscope will introduce additional aberrations, which have not been corrected during the wavefront calibration and consequently make the measured waist larger than its actual value.

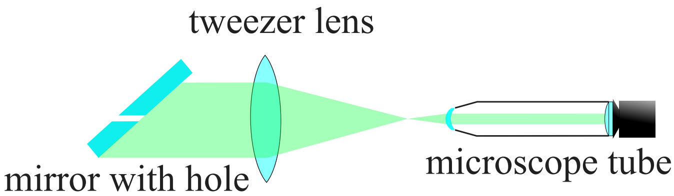

Figure 5.1: Microscope setup for measuring the waist of the tweezers. A microscope is positioned near the focal point of the tweezer lens to magnify the tweezer array. The microscope consists of an objective lens and an eyepiece mounted on the same lens tube, providing a total magnification of 22.2×.

The second-moment measurement is frequently used in this thesis, the information about this method is taken from Ref. [34]. Let's consider the intensity profile of the measured beam in the transverse plane $I(x, y)$. The centroid (x_c, y_c) of the beam is defined as:

$$x_c = \frac{\int\int \mathrm{d}x\mathrm{d}y I(x,y)x}{\int\int \mathrm{d}x\mathrm{d}y I(x,y)}, \tag{5.1}$$

$$y_c = \frac{\int\int \mathrm{d}x\mathrm{d}y I(x,y)y}{\int\int \mathrm{d}x\mathrm{d}y I(x,y)}. \tag{5.2}$$

The inertia matrix I is defined as:

$$I = \begin{pmatrix} \sigma_{xx}^2 & \sigma_{xy}^2 \\ \sigma_{yx}^2 & \sigma_{yy}^2 \end{pmatrix}, \tag{5.3}$$

where

$$\sigma_{xx}^2 = \frac{\int\int \mathrm{d}x\mathrm{d}y I(x,y)(x-x_c)^2}{\int\int \mathrm{d}x\mathrm{d}y I(x,y)}, \tag{5.4}$$

$$\sigma_{xy}^2 = \frac{\int\int \mathrm{d}x\mathrm{d}y I(x,y)(x-x_c)(y-y_c)}{\int\int \mathrm{d}x\mathrm{d}y I(x,y)}, \tag{5.5}$$

$$\sigma_{yy}^2 = \frac{\int\int \mathrm{d}x\mathrm{d}y I(x,y)(y-y_c)^2}{\int\int \mathrm{d}x\mathrm{d}y I(x,y)}. \tag{5.6}$$

For an elliptical beam, the angle θ (azimuthal angle) between the principle axis and the x axis can be derived from the relation

$$\tan(2\theta) = \frac{2\sigma_{xy}^2}{\sigma_{xx}^2 - \sigma_{yy}^2}. \tag{5.7}$$

In the frame of the principle axis, I is diagonalized to $\tilde{I}$ such that

$$I = R(\theta)\tilde{I}R(-\theta), \tag{5.8}$$

with

$$\tilde{I} = \begin{pmatrix} \sigma_{xx}'^2 & 0 \\ 0 & \sigma_{yy}'^2 \end{pmatrix}, \tag{5.9}$$

$$R(\theta) = \begin{pmatrix} \cos\theta & \sin\theta \\ -\sin\theta & \cos\theta \end{pmatrix}. \tag{5.10}$$

Finally, the waist along the major axis and minor axis are defined as

$$w_x = 2\sigma'_{xx}, \tag{5.11}$$

$$w_y = 2\sigma'_{yy}. \tag{5.12}$$

One could easily check that, for a Gaussian beam, the second-moment waists are equal to twice the variances, which are exactly the e^{-2} waists.

Another method for measuring the beam waist is the knife-edge measurement. As illustrated in Fig. 5.2, this classical technique (see Ref. [35]) involves translating a knife edge between the light source and the detector. As the knife moves across the beam, it gradually blocks a portion of the light. By integrating the total radiance recorded on the detector as a function of the knife's position, the resulting signal forms a complementary error function based on the knife's location [36].

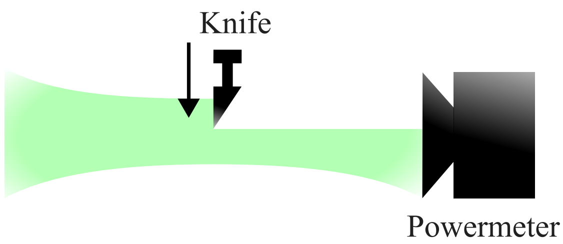

Figure 5.2: The classical setup for knife-edge experiment. It involves translating a knife edge between the light source and the detector. As the knife moves across the beam, it gradually blocks more light. By integrating the total radiance recorded on the detector for various knife positions, the resulting signal forms a complementary error function based on the knife's location.

$$P_{\text{int}}(x) = \frac{P_0}{2}\text{erfc}\left(\frac{x - x_0}{w/\sqrt{2}}\right), \tag{5.13}$$

where

$$\text{erfc}(x) = 1 - \frac{2}{\sqrt{\pi}}\int_0^x \exp(-t^2)\text{d}t. \tag{5.14}$$

In the optical tweezer experiment, the knife-edge measurement is realized without a physical knife. Instead, the spatial light modulator (SLM) is used to scan a blaze grating phase to translate the entire tweezer array, and the pixel boundaries of user-defined regions of interest (ROIs) are considered as the "knife edges" as shown on Fig. 5.3. By translating the entire tweezer array along the x or y axis in the camera frame, and summing the intensity values of the pixels in each ROI, an analog knife-edge measurement is performed. This approach allows us to determine the waists w_x and w_y of each tweezer simultaneously, by fitting the resulting data to Eq. 5.13.

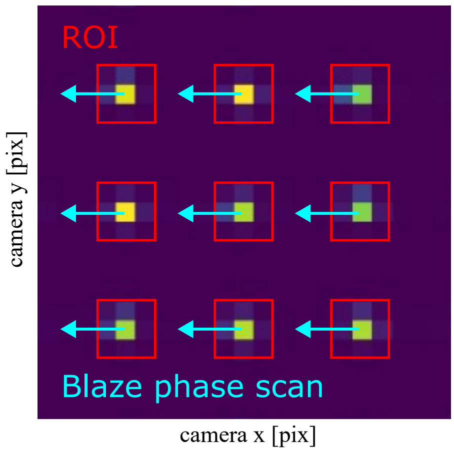

Figure 5.3: Knife-edge measurement for an example 3×3 tweezer array. The red squares are the user-defined regions of interest (ROIs) on which the integrated intensities for each tweezer are obtained. By translating the entire tweezer array along the x axis in the camera frame, and summing the intensity values of the pixels in each ROI, an analog knife-edge measurement is performed.

Fig. 5.4 shows the knife-edge measurement result for one single trap within a 5×5 tweezer array. The blue curve represents the integrated power within the corresponding ROI, while the red curve represents the fitted data. The steepness of the signal drop reveals the waist information: a steeper drop corresponds to a narrower waist. For the full 5×5 tweezer array, the average waist in the x and y directions are measured to be 1.19(5) μm and 1.18(6) μm respectively.

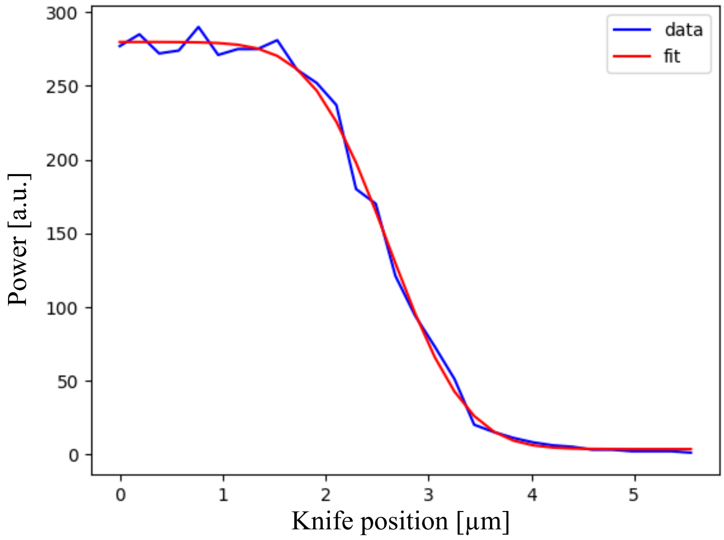

Figure 5.4: SLM knife-edge measurement data fitting for one single trap within a 5×5 tweezer array. The blue curve represents the integrated power within the ROI, while the red curve represents the fitted data. The steepness of the signal drop reveals the waist information: a steeper drop corresponds to a narrower waist. For the full 5×5 tweezer array, the average waist in the x and y directions are measured to be 1.19(5) μm and 1.18(6) μm respectively.

5.1.2 Test of the dichroic mirror and of the mirror with a hole

In the experimental setup, there is a dichroic mirror in between the Keplerian telescope and periscope for reflecting the atom fluorescence. Since the dichroic mirror has only a thickness of 1 mm, it is easy to be bent by the clamp of the mount, making it a potential source of aberrations that deteriorate the tweezer waist. Meanwhile, there is also a mirror with a hole for directing the tweezer light into the tweezer lens. The hole of the mirror crops part of the tweezer beam at the center, which is another source of aberrations. This section shows a study about the influences of the dichroic mirror and the mirror with a hole on the tweezer waist.

- **Dichroic mirror**: When the tweezer light goes through the dichroic mirror, a displacement of the beam occurs due to the thickness of the mirror, which makes the beam off-center. To minimize this effect, we selected a thin dichroic mirror with a thickness of 1 mm. By applying Snell's law, we can calculate the beam displacement for this thin mirror to be 0.45 mm, which is relatively small compared to systematic alignment errors. Regarding the aberrations caused by the deformation of the mirror, they are not pronounced in experiment observations such that the wavefront calibration can compensate for the wavefront distortion and result in an average tweezer waist around 1.2 μm.
- **Mirror with a hole**: The mirror with a hole has a thickness of 6.35 mm to prevent

the surface deformation caused by any stretching or stress, the dimension of the mirror is shown in Fig. 4.3. After the tweezer light is reflected by the mirror, it will lose the central part of the beam due to the hole. It is important to investigate how this hole affects the final tweezer waist. In this thesis, this study first starts by doing a calculation to get a feeling of what result should be expected.

Suppose a Gaussian beam with the field $A(x,y) = A_0 \exp\left(\frac{-(x^2+y^2)}{w_0^2}\right)$ at the input of the mirror, the radius of the central missing spot caused by the hole is r. After the reflection, the field distribution becomes

$$A'(x,y) = A(x,y)(1 - S(x,y)), \tag{5.15}$$

where $S(x,y)$ is an aperture function that

$$S(x,y) = \begin{cases} 1 & \text{if } x^2 + y^2 \leq r^2, \\ 0 & \text{else .} \end{cases} \tag{5.16}$$

According to the wave propagation theory [16], the field at the tweezer focal plane is the Fourier transform of $A'(x,y)$,

$$\mathcal{F}[A'](f_x, f_y) = \mathcal{F}[A](f_x, f_y) - \mathcal{F}[A](f_x, f_y) * \mathcal{F}[S](f_x, f_y). \tag{5.17}$$

The Fourier transform of the Gaussian field $A(x,y)$ is another Gaussian field, and the Fourier transform of the aperture function $S(x,y)$ is proportional to the first order Bessel function of the first kind [18].

$$\mathcal{F}[A](\rho) = A_0 \pi w_0^2 \exp\left(-w_o^2 \pi^2 \rho^2\right) \tag{5.18}$$

$$\mathcal{F}[S](\rho) = \frac{r J_1(2\pi r \rho)}{\rho} \tag{5.19}$$

Both of them have a rotational symmetry, where ρ is the polar coordinate in the Fourier space. The Fourier transform of S reminds us of the result of the diffraction by a circular aperture. It has an Airy disk feature at the center and tails around the disk. The maximal amplitude $2\pi r^2$ is taken when $\rho = 0$ and the first dark ring is taken when $2\pi r \rho = 3.83$, which corresponds to

$$\rho_1 = \frac{3.83}{2\pi r}. \tag{5.20}$$

While for the Fourier transform of the Gaussian beam, the new waist in the spatial frequency domain is

$$w_0' = \frac{1}{w_0 \pi}. \tag{5.21}$$

In real experiment settings, the radius of the hole $r = 0.5$ mm and the theoretical waist of the beam $w_0 = 8.184$ mm. This gives $\rho_1 = 1219.2\ \mathrm{m}^{-1}$, $w_0' = 38.9\ \mathrm{m}^{-1}$ and the maximal amplitude of $\mathcal{F}[S]$ is only $6.28 \times 10^{-6}\ \mathrm{m}^2$. These values indicate that the width of the $\mathcal{F}[S]$ is significantly broader compared to $\mathcal{F}[A]$, while its amplitude is much smaller. This implies that the convolution term in Eq. 5.17 should also exhibit a broader width and smaller amplitude compared to the first term. To check this, we plot the two terms of Eq. 5.17 in Fig. 5.5.

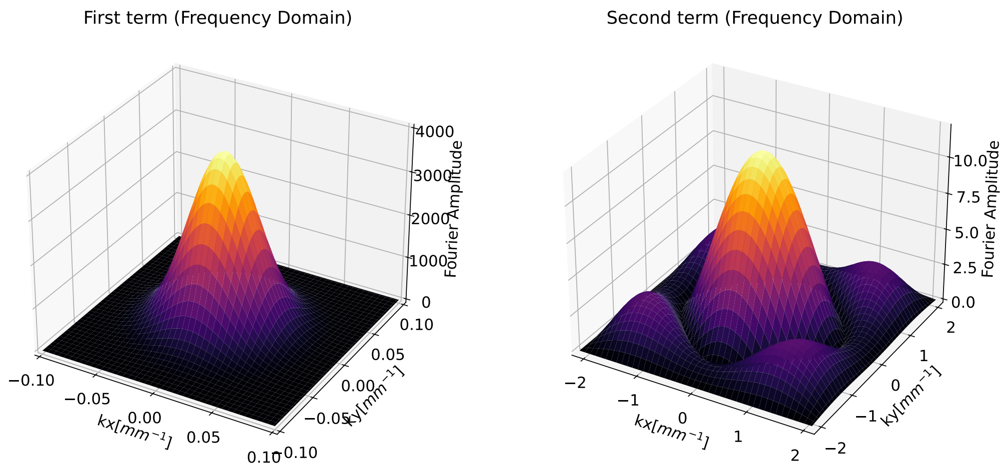

Figure 5.5: The left figure is the plot for the first term and the right figure is for the second term of Eq. 5.17. Note that the z scale of the left plot is much larger than the right plot.

Notably, the amplitude of the first term is indeed significantly larger than the convolution term, thereby making the latter negligible. If we take the norm square of the field $\mathcal{F}[A']$ to get the intensity, the result can be approximated by the norm square of $\mathcal{F}[A]$, which corresponds to the case where no hole is present. In the experiment, the observations agree with the prediction, with the waists always measured to be approximately 1.2 μm.

In summary, the argument above tells us that the dichroic mirror does not cause severe problems besides a small displacement of the beam if it is mounted properly. For the mirror with a hole, the Airy disk introduced by the hole is broad and has a negligible amplitude compared to the Fourier transform of the input Gaussian beam. To demonstrate this, we measured in the experiment a 5×5 tweezer array in the presence of the dichroic mirror and the mirror with a hole. After doing the wavefront calibration, the average waist measured by using the knife edge measurement method is 1.19(7) μm, which is consistent with the waist measured without these two mirrors.

5.1.3 Viewport glass test

The tweezer light is converged into the vacuum chamber through one of the viewports. Nevertheless, the viewport glass is not only another source of aberration but also shifts the location of the tweezer focal plane. This section investigates these effects, both simulations and experimental measurements have been conducted.

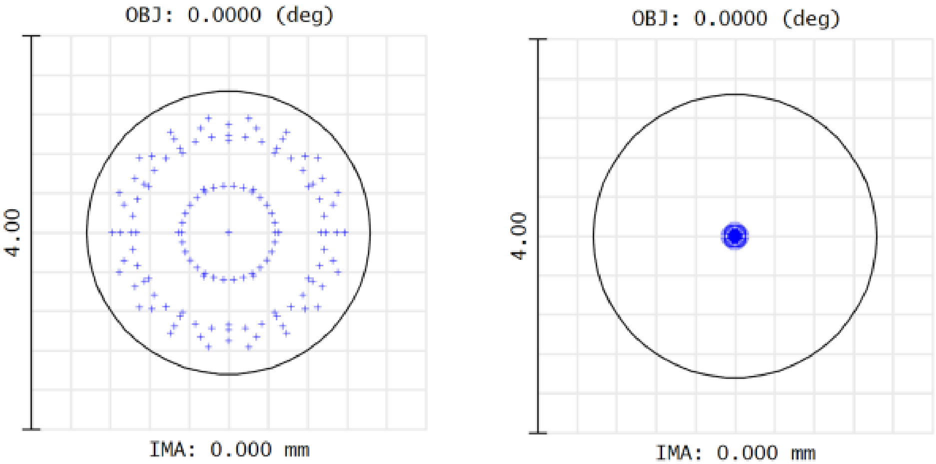

Figure 5.6: Spot diagrams with (left) and without (right) the viewport glass. "OBJ" indicates that the input beam is aligned with the optical axis at a 0-degree angle, while "IMA" marks the geometric center of the image plane. The vertical scale bar represents 4 μm. The blue dots correspond to the ray patterns at the image plane, with the black circle representing the Airy disk. The RMS geometric spot size is 0.921 μm with the viewport glass, compared to 0.067 μm without it. The Airy disk radius remains 1.439 μm in both cases.

Firstly, the system is simulated on Zemax. Fig. 5.6 compares the standard spot diagrams in the focal plane with and without the viewport glass. The Airy disk radius is always 1.439 μm. The root mean square (RMS) geometric spot radius is 0.067 μm without the viewport glass, and it increases to 0.921 μm with the viewport glass. Although the RMS radius increases significantly, it remains smaller than the Airy disk radius, indicating that the system remains within the diffraction-limited regime.

Additionally, the focal plane shift is also measured using Zemax. Without the viewport glass, the focal plane is 46.751 mm from the rear surface of the tweezer lens. When the viewport glass is introduced, this distance increases to 47.397 mm, resulting in a focal plane shift of 0.646 mm.

In the experimental verification, the camera housing has a length of 30 mm from its opening to the sensor. This size constraint prevented us from placing the camera sensor directly at the focus when the viewport glass is present between the tweezer lens and the camera. For this reason, the tweezer array is recorded by using the microscope configuration depicted in Fig. 5.1, and the beam waist is determined by the second-

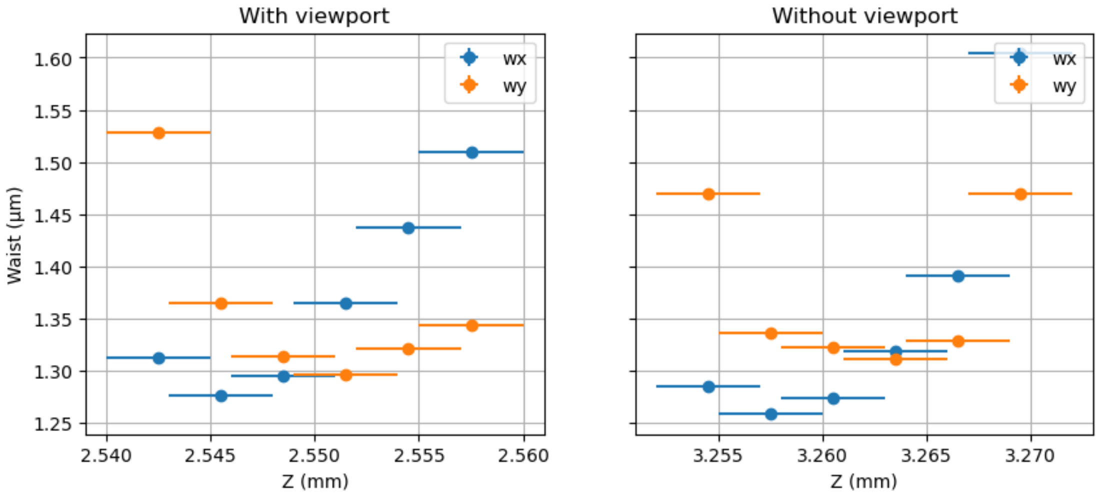

Figure 5.7: The waist scan along z axis without(left) or with(right) the viewport glass. The large horizontal error bar is due to the systematic error of the translation stage.

moment method.

Fig. 5.7 illustrates the beam waist variation near the focus along the axial direction for both cases. It is important to point out that the scale unit of the translation stage is 10 μm, which is larger than the Rayleigh range ($z_R = 8.5\ \mu$m). This large-scale unit made it challenging to precisely position the camera sensor close to the exact focus, leading to a significant systematic error bar (5 μm) along the x-axis of the plot. Despite this, the data indicates that the waist near the focus does not change significantly between the two cases.

Due to time constraints, we could not measure the waist at the focus with higher precision, which could have been achieved with a translation stage of higher resolution. For the focus shift, our measurements indicate a displacement of 0.71(1) mm, which is larger than the value predicted by Zemax. The reason for the discrepancy remains unknown.

In summary, the viewport glass shifts the tweezer focus by approximately 0.7 mm but does not significantly alter the tweezer waist.

5.1.4 Ring electrodes light cropping test

In the vacuum chamber, a pair of ring electrodes are used to excite the atoms into a circular Rydberg state, as shown in Fig. 5.8(a). The dimension of the ring electrodes is 30 mm $\times$ 30 mm and the spacing between them is 6.873 mm according to the technical drawing. When the tweezer light is focused into the vacuum chamber along the z direction, the front edges of those electrodes may obstruct portions of the light that extend outside the enclosed space. This cropping could potentially enlarge the tweezer waist or, more critically, cause the charging of the electrodes. Therefore, it is essential to quantify how much the tweezer waist increases when light cropping occurs.

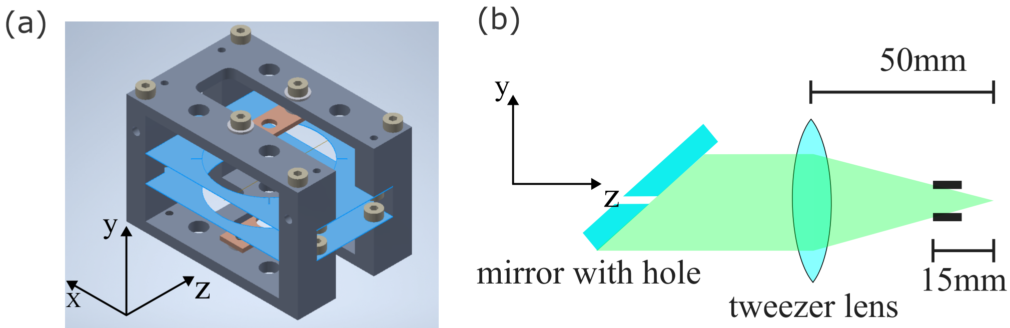

Figure 5.8: (a). The ring electrodes [12], highlighted in the figure, have dimensions of 30 mm × 30 mm and a spacing of 6.873 mm between them. As the tweezer light converges into the vacuum chamber along the z direction, the front edges of the electrodes may crop light that falls outside the enclosed space. (b). Experimental setup for testing light cropping by the ring electrodes. A cylindrical lens mount from Thorlabs (illustrated in black) simulates the electrodes. The tweezer light is focused by the tweezer lens and passes between the two blades of the cylindrical lens mount.

Fig. 5.8(b) shows the experimental setup for the test. A cylindrical lens mount (Thorlabs, part no. CYCPA) was used to simulate the electrodes. After the tweezer light is converged by the tweezer lens, it passes between the two blades of the cylindrical lens mount (illustrated in black). Due to the same constraint of the camera housing, it is impossible to measure the tweezer waist when positioning the cylindrical lens mount at the location where the ring electrodes are. To mitigate this problem, a microscope is placed after the tweezer lens focus to image the tweezer array.

By moving the cylindrical lens mount along the inverse z direction, different portions of the beam are cropped by its blades. For each position, the second-moment method is used to measure the waist of a single tweezer. Fig. 5.9 shows the measured waist as a function of the distance from the blade to the focal plane. When the blades are at 0 mm (aligned with the focal plane), no light is cropped, and this data point serves as a reference waist in the absence of cropping.

As the cylindrical lens mount is moved away from the tweezer plane, its blades progressively block more light in the x direction, causing the waist w_x to increase while the w_y remains relatively constant (with slight fluctuations). According to the technical drawing, the theoretical distance from the edge of the electrodes to the focal plane is 15 mm. When moving the cylindrical lens mount from the focal plane to this point, the waist increases from 1.21(1) μm to 1.26(1) μm. If the cylindrical lens mount is displaced with an additional distance of approximately 3 mm from this point, the waist only increases to 1.27(1) μm.

In conclusion, the increase in tweezer waist due to the cropping of the electrodes is approximately 4%, which is relatively small. In addition, this result remains true with a tolerance of 3 mm for the location of the electrodes.

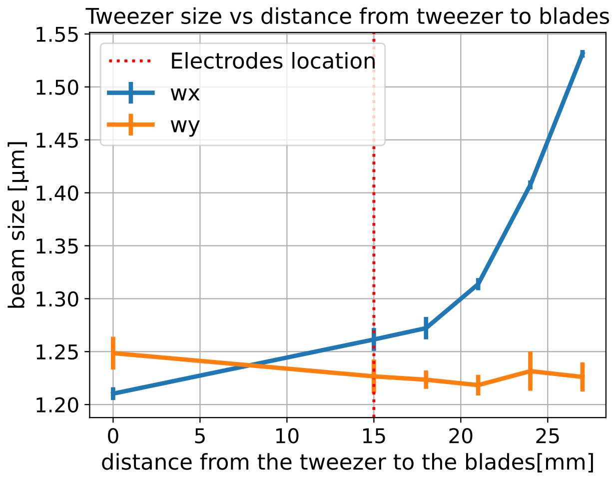

Figure 5.9: The measured tweezer waist as a function of the blade position. The theoretical distance from the edge of the electrodes to the tweezer plane is 15 mm.

5.2 Tweezer focus shift methods

For all the topics discussed above, the tweezer array is located at the focal plane of the tweezer lens. However, in real experiment settings, it is beneficial to have some tunability of the z (axial) location of the optical tweezer array, since it allows us to overlap the tweezer array with the MOT more easily. This section introduces two methods to shift the location of the focus. The first method is by displacing the first lens of the Keplerian telescope away from the initial position, while the second method is by imprinting a lens phase mask on the SLM to effectively form a virtual lens.

5.2.1 Lens displacement method

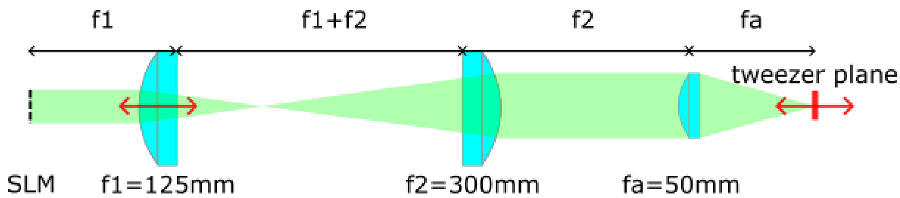

Figure 5.10: The layout of the Keplerian telescope lenses f_1 and f_2 the tweezer lens f_a. By moving the f_1 forward or backward, we can accordingly change the location of the tweezer focal plane.

Recall in the setup, there is a Keplerian telescope that expands the beam before the tweezer lens, as shown in Fig. 5.10. By moving the first lens of the telescope forward, the spacing in between the telescope increases to a value larger than $2f$, and the emerging light after the telescope is a converging light, consequently, the focal plane for the tweezer lens is moved forward. Conversely, by moving the lens backward, the tweezer focal plane is shifted backward accordingly. It is interesting to determine, for a given tweezer plane shifting distance, by how much the first lens of the telescope needs to be moved. Also, studying the permitted moving range of the tweezer plane while keeping a good image quality of the tweezer is of great importance.

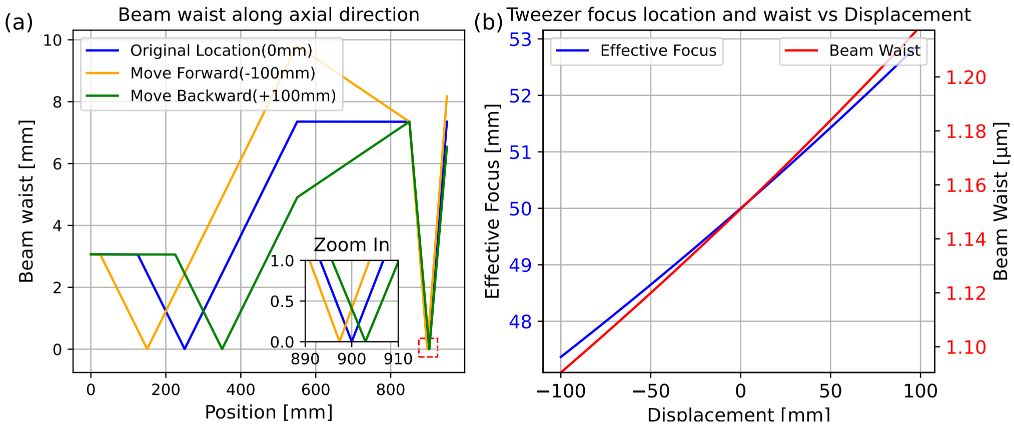

Figure 5.11: (a). The variation of the waist through the optical system. Each line corresponds to different displacement of the first lens of the telescope. (b). The tweezer focus location and waist as a function of the displacement of the first lens.

The ABCD matrix [37] for the Gaussian beam was used to simulate the light propagation through the optical system. Fig. 5.11(a) shows the waist variation of the beam along the axial direction for 3 cases: (1). the first lens is moved forward by 100 mm (yellow). (2). no change in position (blue). (3). the first lens is moved backward by 100 mm (green). The inset shows the waist size in the vicinity of the focus position, by translating the telescope lens forward or backward by 100 mm, the location of the tweezer plane is shifted accordingly by ± 2.8 mm. Fig. 5.11(b) shows the focus location (blue) and the waist size (red) for different displacement amounts of the telescope lens. The slope for the blue line is 0.0276, this means if we displace the telescope lens backward by 100 mm, the tweezer focus will be moved by 2.7 mm. The red line indicates that this method does not significantly alter the waist size of the focus.

However, in real experiment settings, the action of moving the telescope lens will bring more aberration into the optical system. The same simulation was conducted on Zemax to study the effect of the aberration. In Fig. 5.12, the blue curve shows the focus location of the tweezer lens and the red curve represents the root mean square of the geometric spot size divided by the Airy disc radius. The slope for the blue line is 0.0281, which is approximately in agreement with the result from the previous simulation. By limiting ourselves under the constraint that the RMS of the geometric spot size is less than the radius of the Airy disk, the permitted translation range of the telescope lens is around ± 25 mm, corresponding to a focus shift of approximately ± 0.7 mm for the tweezer.

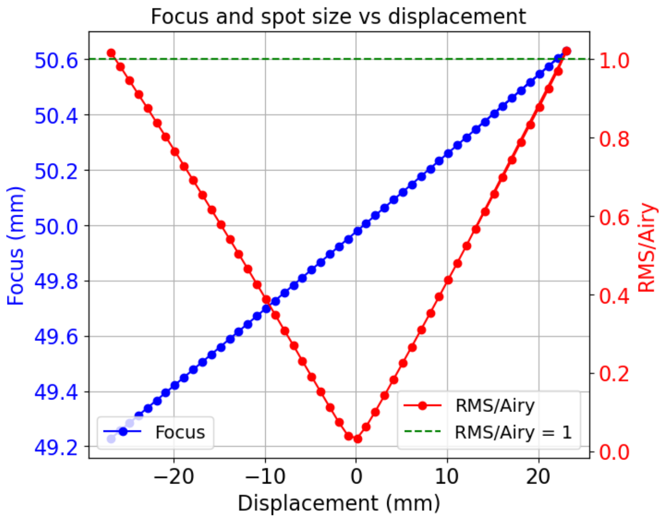

Figure 5.12: The variation of the tweezer focus location and the root mean square of the geometric spot size divided by Airy disk radius for different displacements of the telescope lens.

5.2.2 Virtual lens method

Another method we can apply to shift the focus of the tweezer is by imprinting the phase of a lens on the SLM. According to Eq. 2.12, by applying the phase $\phi(\delta z) = \frac{\pi \delta z M^2}{\lambda f^2}(x^2 + y^2)$ on the SLM, the focus can be shifted by δz.

To demonstrate this method, a simulation on Zemax was conducted by using its Zernike polynomial surface. This surface type allows users to implement a phase mask by specifying coefficients for a finite number of Zernike polynomials. Among these terms, the Z_2^0 term corresponds to the defocus. Fig. 5.13 (a) shows how the focus location and RMS of geometric spot size change by varying the coefficient of Z_2^0. Under the same constraint that the RMS spot size is smaller than the Airy disk radius, the focus location can be altered by approximately ± 0.6 mm.

One advantage of working with an SLM is that we can correct the primary spherical aberration by applying another term Z_4^0. Fig. 5.13 (b) shows the simulation result when the optimal coefficients of Z_4^0 are applied. Keeping correcting the primary spherical aberration while scanning the Z_2^0 coefficient, the RMS spot size remains nearly constant across different values of Z_2^0. This suggests that the focus location can be modified by any amount without degrading the tweezer quality. However, this is not entirely accurate in practice. As the coefficient increases, the phase gradient on the SLM also increases, leading to a reduction in diffraction efficiency.

Besides the simulation, an experiment has been performed to demonstrate the virtual lens method. To ensure the validity of this method, the following parameters need to be checked:

- By applying a virtual lens phase $\phi(\delta z)$ with theoretical defocus δz on the SLM,

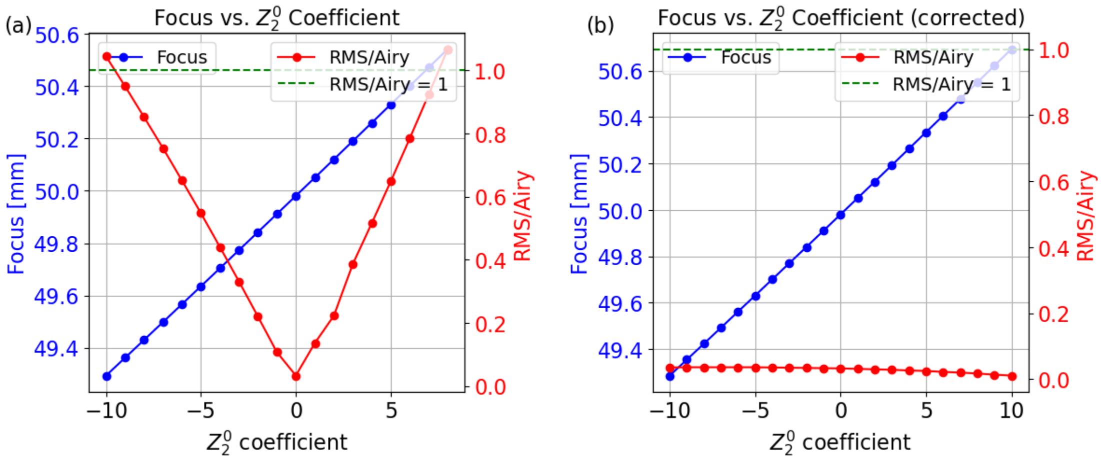

Figure 5.13: The results of the virtual lens imprinting method. (a) Shifting the tweezer focus by only applying the defocus term Z_2^0. The achievable focus shift range is ± 0.6 mm while keeping the RMS spot size smaller than the Airy disk radius. (b) In addition to the defocus term Z_2^0, the Z_4^0 Zernike polynomial is applied to correct the spherical aberration. The beam waist remains constant across the focus shift.

what is the corresponding focus shift realized in the experiment?

- By shifting the focus location at different amounts, what is the corresponding waist size at the focus?

In the experiment, the camera is placed near the tweezer lens focus and a wavefront calibration is performed such that it corrects the alignment errors and out-of-focus errors of the camera. After the calibration, the camera is assumed to be in the focus of the tweezer lens and its alignment is good. The general verification procedure consists of:

1. Imprint a phase mask $\phi(\delta z)$ on the SLM to alter the focus location by theoretical value δz.
2. Turning the screw of the translation stage of the camera to move it to the new focus.
3. The focus shift amount d is measured to be the distance between the initial position z and final position z' of the camera.
4. The waist at the focus is measured at the final camera position.

However, consider a tweezer waist of 1.2 μm, the corresponding Rayleigh range would be 8.5 μm, which is smaller than the unit step of the translation stage 10 μm. Limited by the precision of the translation stage, a large systematic error 5 μm (which is assumed to be half the unit step) is present for the camera's final position z'. In addition, it complicates the measurement of the waist size, since positioning the camera at the new focus is difficult. For these reasons, the normal procedure described above does not apply in this case.

Therefore, a passive measurement method is applied to tackle the problems above:

1. Instead of translating the camera to match the location of the new focal plane, the camera is first translated by a known amount d, which is much larger than the unit step of the translation stage.
2. The SLM scans the phase $\phi(\delta z)$ to shift the focus by different theoretical values δz.
3. For each phase mask $\phi(\delta z)$, a knife-edge measurement is effectuated to measure the waist of the light spot recorded by the camera.
4. The Gaussian beam waist variation equation 5.22 [38] is used to interpolate the location of focus as well as the waist.

$$w(z) = w_0\sqrt{1 + M^2\left(\frac{z - z_0}{z_R}\right)^2}, \tag{5.22}$$

where w_0 is the focus waist, z is the axial coordinate, z_0 is the axial coordinate of the waist, z_R is the Rayleigh range and M^2 is the quality factor.

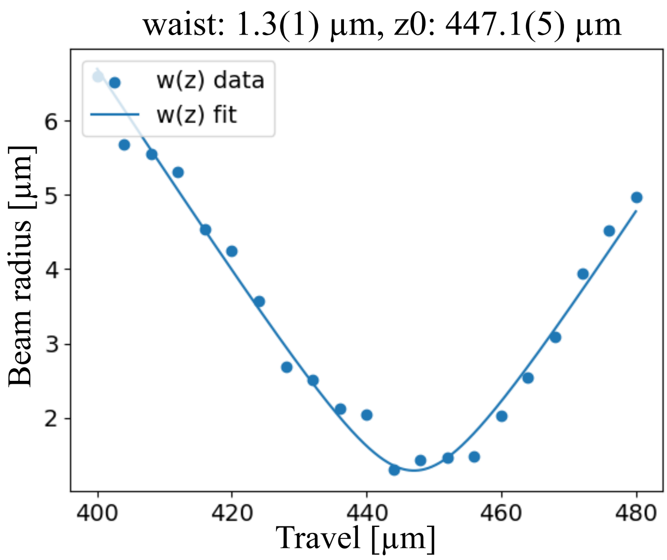

Figure 5.14: The virtual lens scan of δz when the camera is translated by 500 μm. The fitting result indicates that the waist 1.3(1) μm is obtained when δz is 447.1(5) μm.

In this passive measurement, the increment of δz implemented in the phase scan is more uniform compared to the increment of using a translation stage, and it can be made as small as possible, ensuring the precision and the reliability of the waist curve fitting. For instance, Fig. 5.14 shows the Gaussian beam curve fitting when the camera is translated by 500 μm. The x axis is the theoretical focus shift δz of the virtual lens phase $\phi(\delta z)$ and the y axis is the measured waist. The figure indicates the focus displacement determined by the SLM is 447(1) μm, and the measured waist at the focus is 1.3 μm.

Fig. 5.15 presents the fitting results by displacing the camera by various amounts. The x axis is the distance d of the camera from its original location, the blue data points are theoretical value δz determined by SLM, and the red data points are the corresponding waists at focus. The linear fit of δz versus d has a slope of 0.878(4). It suggests that to implement a target defocus d in the experiment, we need to apply a phase $\phi(\delta z)$ with $\delta z = 0.878d$. The discrepancy between the expected defocus δz and the realized one d might be explained by the following aspects:

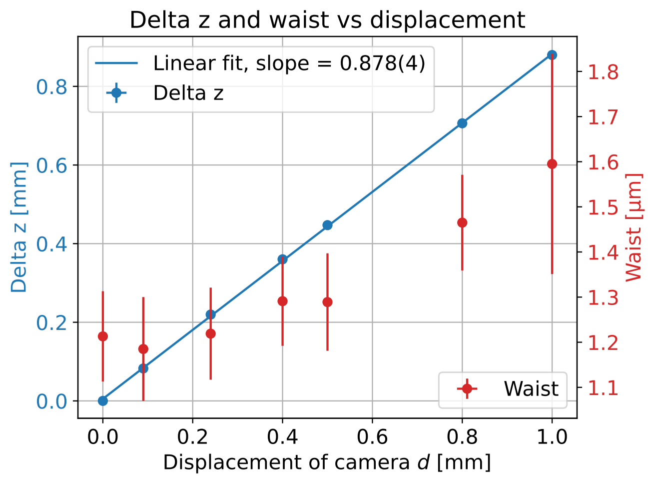

Figure 5.15: The camera displacement δz determined by SLM and the waist when the camera is translated by different amounts. The focus can be shifted by ± 0.5 mm while maintaining the tweezer waist smaller than 1.3 μm.

1. The $\pm 2\%$ error for the effective focal length (EFL) of telescope lenses $f_3 = 150$ mm and $f_4 = 400$ mm (see Fig. 4.1) leads to a departure from the theoretical magnification factor $M = 400/150$.
2. The tweezer lens $f = 50$ mm is designed for $\lambda = 355$ nm instead of $\lambda = 532$ nm, while it is assumed that $f = 50$ mm in the calculation of the phase $\phi(\delta z)$.

Regarding the waist size, the figure indicates that the waist is initially around 1.2(1) μm and increases to 1.6(3) μm when the focus is shifted by 1mm. When maintaining the tweezer waist smaller than 1.3 μm the focus can be shifted by ± 0.5 mm.

The spherical aberration correction for the virtual lens by applying the Z_4^0 term of the Zernike polynomials is also demonstrated. The procedure for this aberration correction is following:

1. Translate the camera by d and scan the δz using SLM to determine the phase mask $\phi(\delta z)$ that shifts the focus onto the camera.
2. Sit at the focus by applying the phase mask $\phi(\delta z)$ obtain from previous step and effectuate a scan for Z_4^0 Zernike phase.
3. Perform a knife-edge measurement for each of those Z_4^0 coefficients to measure the waist of the light spot recorded in the camera.
4. The coefficient Z_4^0 for correcting the spherical aberration is taken at the minimum value of the measured waist.

The procedure above is conducted first for some small displacements $d < 500$ μm. However, the additional Z_4^0 Zernike phase mask does not decrease the measured waist. The reason may be the spherical aberration is not significant for small displacements d. Moreover, the imperfections in the Zernike phase mask likely reduce its effectiveness, making the potential benefit of applying the additional Z_4^0 coefficient smaller than the associated losses.

For large displacement value $d \geq 800$ μm, the benefit of Z_4^0 starts to manifest. For instance, Fig. 5.16 (a) shows the waist size variation while scanning the Z_4^0 in the interval $[-2, 2]$ rad in the case $d = 1$ mm. There is a waist minimum around $Z_4^0 = -0.3$ rad. Fig. 5.16 (b) presents another scan of Z_4^0 in the range $[-1, 0]$ rad with a higher scan rate. A minimal waist of 1.4(1) μm is observed around $Z_4^0 = -0.38$ rad, it is smaller than the value 1.6(3) μm when no spherical aberration correction is applied. This demonstrates that applying the Z_4^0 coefficient phase mask indeed corrects the spherical aberration of the virtual lens. Nevertheless, it is not able to recover the waist back to its original value 1.2 μm due to the imperfection of Z_4^0 Zernike phase and higher-order spherical aberrations of the virtual lens.

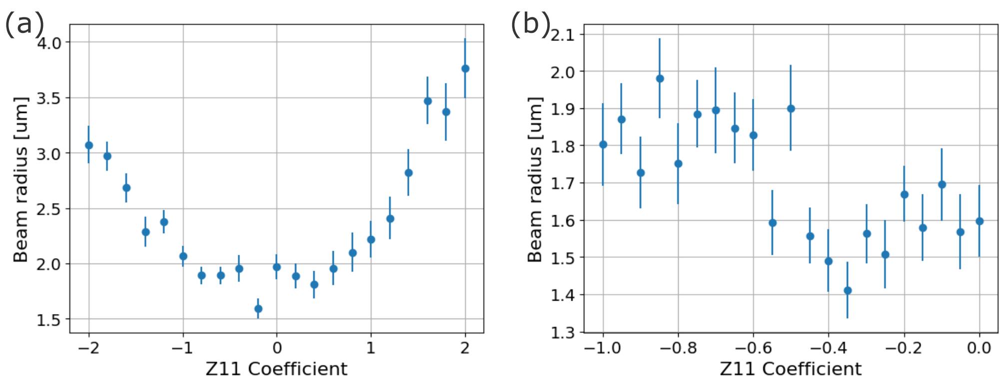

Figure 5.16: (a) The measured waist for a broad scan of Z_4^0 in the interval $[-2, 2]$ rad. (b) The measured waist for a finer scan of Z_4^0 in the interval $[-1, 0]$ rad.

In summary, this section presents the virtual lens method of shifting the tweezer focal plane by doing both a Zemax simulation and an experimental verification. The simulation suggests that the focus can be shifted by ±0.6 mm under the constraint that the RMS spot size is smaller than the Airy disk radius, while the experiment shows the focus can be altered by ±0.5 mm if maintaining the waist size smaller than 1.3 μm. It also demonstrates that scanning the Z_4^0 term of Zernike polynomials corrects the spherical aberration of the virtual lens. However, it only works when the defocus amount is large.

5.3 Diagnostic camera

During the setup characterization, the tweezer array was observed by a camera or microscope located at the focus, which is referred to as the tweezer camera. However, after integrating the tweezer setup within the vacuum apparatus, the tweezer array is formed inside the vacuum chamber, making direct imaging impossible. Instead, the diagnostic camera is used to monitor the status of the tweezer array.

Analyzing the differences between the wavefront calibration phase masks obtained from the tweezer camera and the diagnostic camera is beneficial. Firstly, this comparison provides insight into the differences in aberrations experienced by the tweezer light and diagnostic light, given that they should share the same aberrations up to the mirror with a hole. Secondly, if the aberration difference between the two cameras remains stable over time and is relatively insensitive to environmental perturbations, it allows us to reconstruct the correction phase mask for the tweezer array using the diagnostic camera. In particular, this is achieved by adding the stable phase difference to the wavefront calibration phase of the diagnostic camera.

5.3.1 Spot shape

We first applied the wavefront calibration result of the tweezer camera and generated a 5×5 tweezer array. Fig. 5.17 (a) shows one representative tweezer image recorded in the diagnostic camera. It exhibits a larger waist size along the x-axis, accompanied by a tail. Both the second-moment measurement and the knife-edge measurement were performed to measure the tweezer waists. Tab. 5.1 presents the measurement results after accounting for the magnification factor of the diagnostic lens with respect to the tweezer lens.

	Second moment	Knife edge
$w_x(\mu\text{m})$	2.52(16)	1.88(28)
$w_y(\mu\text{m})$	1.48(9)	1.31(8)

Table 5.1: The waist measurement results in the diagnostic camera.

The results indicate that the beam waists measured using the second-moment method are generally larger than those obtained via the knife-edge measurement. This discrepancy arises because the second-moment method calculates only the intensity distribution, while the knife-edge method involves fitting the data to Eq. 5.13, where the probed beam is assumed to be Gaussian. Despite this difference, both methods consistently show that

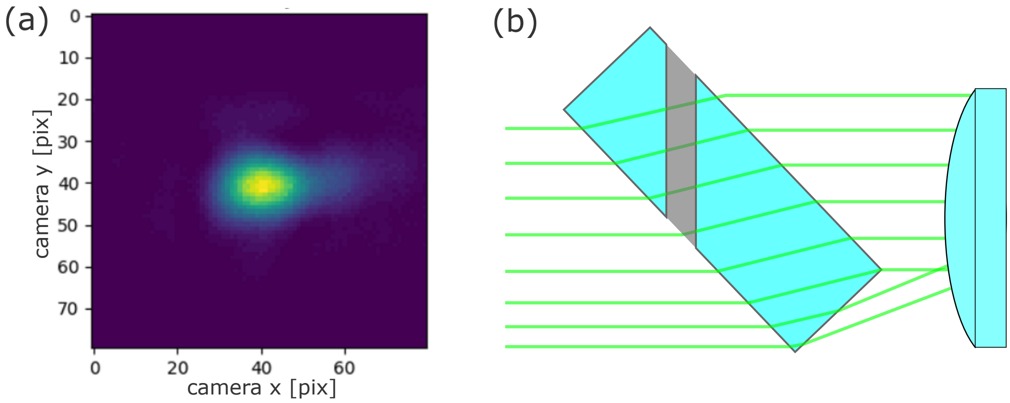

Figure 5.17: (a) A picture of a typical tweezer spot observed in the diagnostic camera. It exhibits a larger waist size along the x-axis, accompanied by a tail. (b) The sources of the deteriorated tweezer image recorded in the diagnostic camera: 1. The scattering due to the edge of the hole. 2. The bottom part of the light is refracted by the lateral surface of the mirror. 3. The thickness of the mirror leads to an off-centered beam with respect to the focusing lens.

w_x is significantly larger than w_y. The ellipticity and the beam tail can be attributed to three key factors, as illustrated in Fig. 5.17 (b):

1. **Impact of the Diagnostic Mirror**: The mirror has a through-hole aligned along the x-direction in the camera frame. Light passing through the hole may be scattered when it encounters the rough surface at the edge of the hole, causing a loss of intensity in that region after transmission through the mirror.

2. **Light Refraction at the Mirror's Lateral Surface**: While most of the light continues in a straight path after transmission, the lower portion of the beam is refracted by the mirror's lateral surface. This refraction causes part of the beam to deviate at an angle, resulting in a cropping of the beam.

3. **Off-Center Rays and Aberrations**: The light that does not travel through the hole or encounter the lateral surface of the mirror experiences a shift upwards after transmission, causing the beam to become off-center. When this off-center beam passes through the lens, it introduces aberrations that further distort the beam profile.

A wavefront calibration is then performed for the diagnostic camera. When applying the obtained correction phase mask, the tweezer array spot observed in the diagnostic camera looks tight while the spots in the tweezer camera are strongly affected, see Fig. 5.18. The average waist of the array in the perspective of the tweezer camera is measured to be 1.96(9) μm.

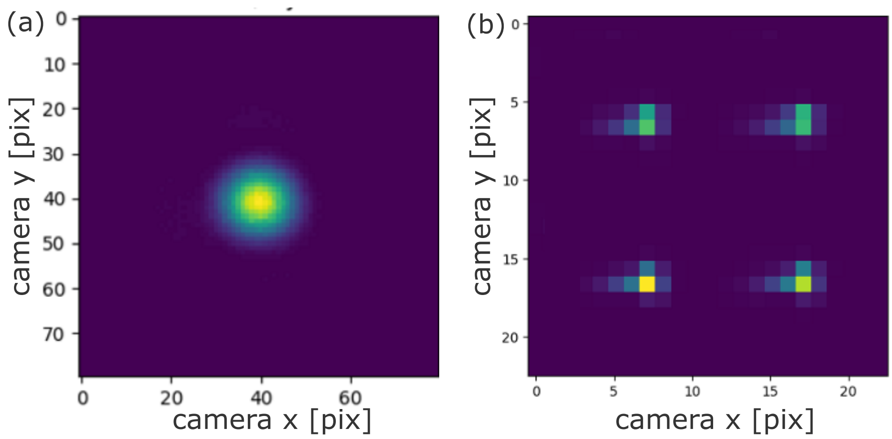

Figure 5.18: (a) A representative spot in the diagnostic camera after applying the wavefront calibration result of the diagnostic camera. (b) Corresponding tweezer array observed from the tweezer camera. The tweezer quality is significantly degraded.

5.3.2 Phase image stability and correction phase reconstruction

The stability and consistency of the wavefront calibration results for both the tweezer camera and the diagnostic camera enable the reconstruction of the aberration correction phase for the tweezer array. Multiple calibrations were performed on different days to evaluate the stability and insensitivity of the wavefront calibration in the presence of external perturbations, such as installing and uninstalling the diagnostic camera.

Fig. 5.19 and Fig. 5.21 show four different wavefront calibration results for the tweezer camera and diagnostic camera, respectively. Fig. 5.20 and Fig. 5.22 present the corresponding Zernike polynomials coefficient decomposition. The plots follow a chronological order, i.e., the measurements (a) is taken prior to (b), (c), and (d).

- **Tweezer camera**: For the tweezer camera, the wavefront calibration results of (a), (c), and (d) are similar to one another, with (b) exhibiting an overall π offset, making it a negative version of the others. Besides the tilt and defocus terms, the other Zernike polynomial coefficients are stable across all calibrations. The tilt terms, which only shift the spot location, do not affect the image quality and are thus irrelevant for aberration correction. The variation in defocus coefficients is attributed to the different positions of the camera during each calibration, as the wavefront calibration compensates for the errors caused by the fact that the camera is not placed precisely at the focal plane. As expected, vertical astigmatism is the dominant aberration, apart from tilt and defocus, as the primary source of aberration is the curvature of the SLM's backplane. Notably, the magnitude of this coefficient remains stable across all calibrations.

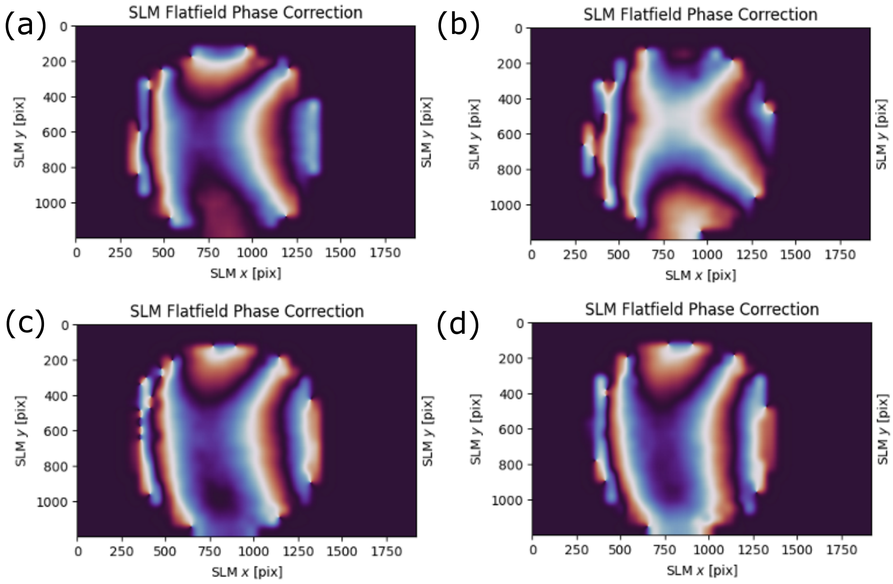

Figure 5.19: The wavefront calibration results performed on different dates for the tweezer camera. The plot follows a chronological order i.e. the measurement of (a) is prior to (b), (c), (d). Image (a), (c), and (d) are similar to each other, while (b) has an overall π offset, making it a negative version of (a), (c), (d).

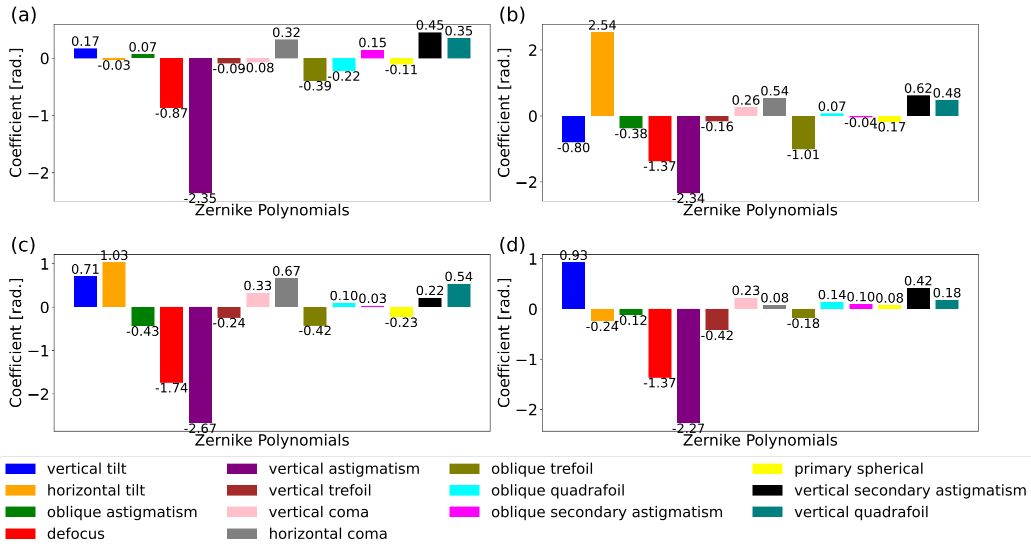

Figure 5.20: Zernike polynomial coefficient decomposition for the tweezer camera's wavefront calibration results. The tilt component is irrelevant to image quality, and variations in the defocus term are caused by the camera being out of focus. Vertical astigmatism is the dominant aberration in all cases.

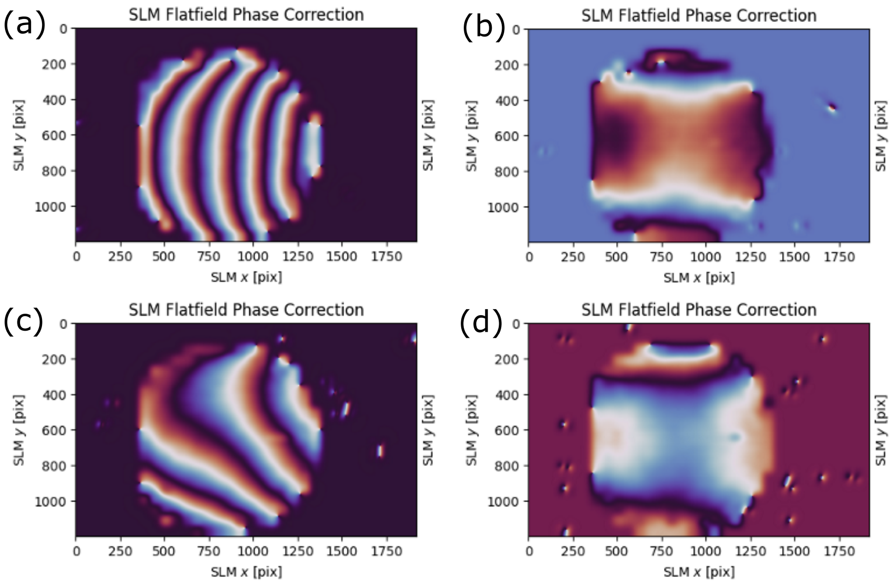

Figure 5.21: Wavefront calibration results for the diagnostic camera, performed on different dates. Phase images (a) and (c) exhibit a strong tilt feature, likely caused by camera misalignment.

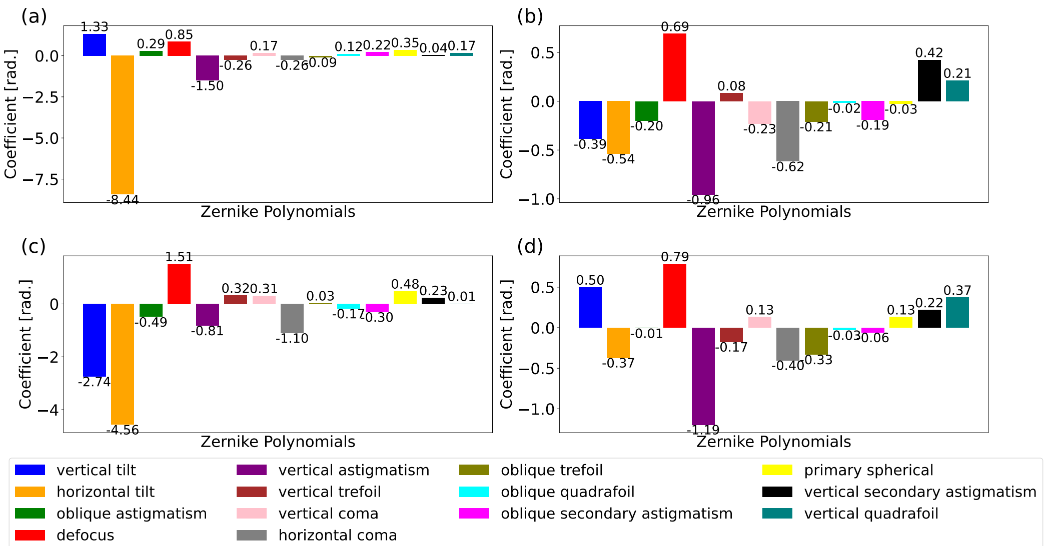

Figure 5.22: Zernike polynomial coefficient decomposition for the diagnostic camera's wavefront calibration results. The vertical astigmatism coefficient fluctuates between −0.81 rad to −1.50 rad, with the cause of this fluctuation remaining unclear.

- **Diagnostic camera**: For the diagnostic camera, phase images (a) and (c) exhibit a strong tilt feature, likely caused by misalignment, where the light does not strike the camera sensor perpendicularly. Similar to the tweezer camera, variations in the defocus coefficients arise due to the camera being out of focus during each calibration. Vertical astigmatism remains the dominant aberration after accounting for tilt and defocus, but its magnitude fluctuates between −0.81 rad and −1.50 rad, the cause of which is still unclear.

For the reconstruction of the aberration correction phase, the tweezer camera phase image (d) is subtracted by the corresponding diagnostic camera phase image (d) to yield the phase difference $\Delta\phi$. By adding $\Delta\phi$ to diagnostic phase images (a), (b), (c), and (d) respectively, the aberration correction phases for the tweezer array are reconstructed. Table 5.2 shows the measured waists of a generated 5×5 tweezer array when applying these reconstructed phase masks. Except for (a), the measured waists for (b), (c), and (d) are around 1.5–1.6 μm. Even though these values are larger than the 1.19(6) μm obtained by directly performing the wavefront calibration for the tweezer camera, it still represents an improvement over the waist size 1.96(9) μm when using the unprocessed phase mask from the diagnostic wavefront calibration.

	(a)	(b)	(c)	(d)
$w_x(\mu\text{m})$	1.96(13)	1.50(10)	1.64(11)	1.56(11)
$w_y(\mu\text{m})$	2.00(30)	1.60(10)	1.61(13)	1.48(14)

Table 5.2: Measured waist for the correction phase reconstructed from diagnostic phase images(a), (b), (c), and (d).

In conclusion, aside from the tilt and defocus components, the aberration phase images demonstrate stability across individual calibrations for the tweezer camera. For the diagnostic camera, however, there is an inconsistency in the vertical astigmatism, the cause of which remains unclear. Even though the correction phase reconstruction method does not fully recover the optimal waist size of 1.2 μm, it offers an improvement compared to directly using the unprocessed wavefront calibration results from the diagnostic camera.

5.4 Aberration path

The phase images obtained during wavefront calibrations contain information about the aberrations in the optical path up to the calibration point. In this section, the wavefront calibrations are conducted at various locations along the optical path, and the aberrations of each element can be isolated by subtracting the corresponding phase images. The resulting phase difference image helps analyze the aberrations caused by individual optical components.

To guarantee the reliability of the aberration isolation, precise camera alignment and minimal aberration introduced by the camera lens are essential. Inconsistency in alignment and out-of-focus amount of the camera between two calibrations can result in tilt and defocus components in the phase image difference. The tilt component only shifts the location of the tweezer spot without degrading image quality and can be omitted in the aberration analysis. However, the defocus component alters the tweezer waist location, causing a larger spot size measured on the camera.

In our experiment, wavefront calibrations were performed at the following locations:

(a) After reflection from the SLM.

(b) After passing through the Keplerian telescope.

(c) After the tweezer lens, without the presence of the dichroic mirror or mirror with a hole.

(d) After the tweezer lens, with only the mirror with a hole.

(e) After the tweezer lens, with both the dichroic mirror and the mirror with a hole inserted.

(f) After passing through the diagnostic path.

To extract the aberrations of specific optical components:

- Subtracting (a) from (b) isolates the aberration introduced by the Keplerian telescope.
- Subtracting (b) from (c) yields the aberration introduced by the tweezer lens.
- Subtracting (d) from (e) provides the aberration introduced by the dichroic mirror.
- Subtracting (b) from (f) isolates the aberration of the mirror with a hole and the diagnostic path.

After obtaining the phase differences, we unwrap the phase and perform a Zernike coefficient fitting, Fig. 5.23 shows the corresponding results. The following presents the analysis of the aberrations of each isolated component. As previously mentioned, the tilt and defocus components are not irrelevant to the optical elements' aberrations. Therefore, they are excluded from further discussion.

- **Keplerian telescope**: The dominant aberration of the Keplerian telescope is vertical astigmatism, which could be attributed to the tight clamping of mirrors within the U-shaped telescope. Additionally, there is also the primary spherical aberration, likely resulting from the large beam size in the telescope, which makes the paraxial approximation inaccurate.
- **Tweezer lens**: A significant contribution of vertical coma is observed for the tweezer lens. This may be caused by the non-orthogonal incident angle of the light entering the tweezer lens when applying a blazed phase during wavefront calibration. The tweezer lens also introduces the primary spherical aberration.

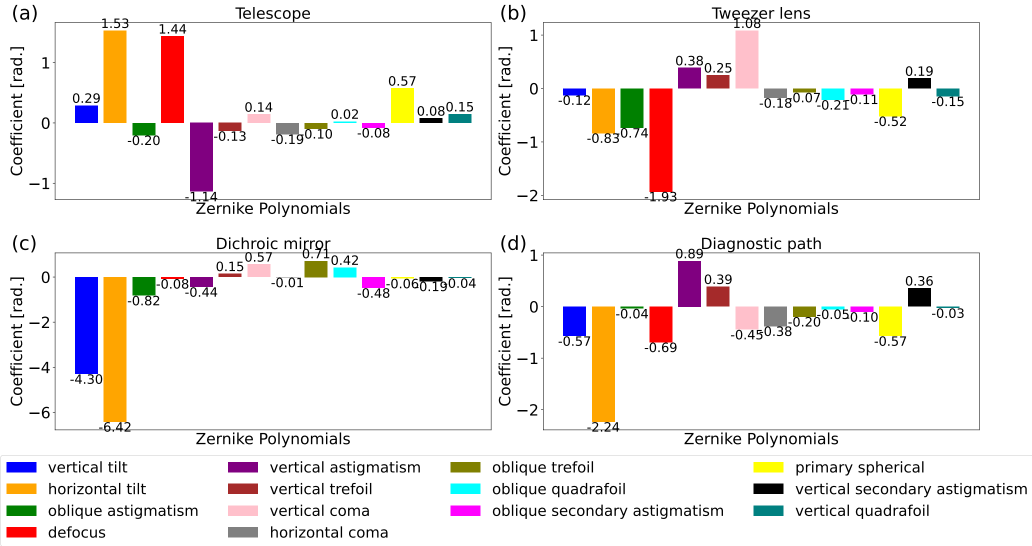

Figure 5.23: The Zernike decomposition of the measured aberrations of the Keplerian telescope, tweezer lens, dichroic mirror, diagnostic path.

- **Dichroic mirror**: No spherical aberration appears for the mirror. However, the mirror introduces a combination of other aberrations, such as astigmatism, coma, and quadrafoil, likely due to the mirror surface distortion.
- **Diagnostic path**: Astigmatism is again a dominant aberration, possibly due to the tight clamping of the mirrors and the mirror with a hole in this path. Additionally, coma and spherical aberration are introduced by the diagnostic camera lens.

In summary, the aberrations along the optical path were effectively isolated and analyzed using wavefront calibrations at different locations. Vertical astigmatism is identified as the dominant aberration in the Keplerian telescope and diagnostic path, likely due to mechanical clamping issues of mirrors. Additionally, spherical aberration in the Keplerian telescope and vertical coma in the tweezer lens are attributed to beam size and misalignment during calibration. These results provide insights for improving the system's optical performance.

Chapter 6

Conclusion

This thesis has carried out the tasks of designing, building, and characterizing an optical tweezer setup for trapping calcium atoms.

In the first part, the focus was on designing the experimental setup. By making use of the mirror with a hole, the tweezer setup successfully enabled a combination of the tweezer light and the MOT beam with minimal modification to the existing MOT setup. Additionally, it provides the necessary tools for collecting atom fluorescence.

The second part investigated the influence on the tweezer waist of components like the dichroic mirror for fluorescence, mirror with a hole, viewport glass, and ring electrode. Both simulations and experimental measurements confirmed that these components did not significantly degrade the optical tweezers, and the tweezer waist remained below the upper limit of 1.3 μm.

The third part demonstrated two methods of shifting the tweezer plane: the telescope lens displacement method and the virtual lens method. We experimentally implemented the virtual lens method, achieving a tweezer focal shift of approximately ± 0.5 mm, while maintaining the waist below 1.3 μm. In addition, this method also demonstrates the possibility of correcting the spherical aberration by scanning the Z_0^4 term of Zernike polynomials.

The fourth part compared the wavefront calibration results between the tweezer camera and the diagnostic camera. The study demonstrated the stability of the aberrations and proposed a method for reconstructing the correction phase using the diagnostic camera. Although the reconstructed phase did not recover the 1.2 μm, it still produces a waist of approximately 1.6 μm, which is an improvement over using the unprocessed diagnostic wavefront image.

Lastly, the aberrations introduced by individual optical components were analyzed using Zernike polynomial decomposition, providing valuable insights into the optical performance of the setup.

Bibliography

1. Bennett, C. H., Brassard, G. & Ekert, A. K. Quantum cryptography. *Scientific American* **267,** 50–57 (1992).
2. Aspuru-Guzik, A., Dutoi, A. D., Love, P. J. & Head-Gordon, M. Simulated quantum computation of molecular energies. *Science* **309,** 1704–1707 (2005).
3. Bloch, I., Dalibard, J. & Nascimbene, S. Quantum simulations with ultracold quantum gases. *Nature Physics* **8,** 267–276 (2012).
4. Nielsen, M. A. & Chuang, I. L. *Quantum computation and quantum information* (Cambridge university press, 2010).
5. Saffman, M. Quantum computing with atomic qubits and Rydberg interactions: progress and challenges. *Journal of Physics B: Atomic, Molecular and Optical Physics* **49,** 202001 (2016).
6. R. F. Stebbings, F. B. D. *Rydberg States of Atoms and Molecules* (Cambridge University Press, 1983).
7. Saffman, M., Walker, T. G. & Mølmer, K. Quantum information with Rydberg atoms. *Reviews of modern physics* **82,** 2313–2363 (2010).
8. Levine, H. *et al.* High-fidelity control and entanglement of Rydberg-atom qubits. *Physical review letters* **121,** 123603 (2018).
9. Hulet, R. G. & Kleppner, D. Rydberg atoms in" circular" states. *Physical review letters* **51,** 1430 (1983).
10. Kleppner, D. Inhibited spontaneous emission. *Physical review letters* **47,** 233 (1981).
11. Hulet, R. G., Hilfer, E. S. & Kleppner, D. Inhibited spontaneous emission by a Rydberg atom. *Physical review letters* **55,** 2137 (1985).
12. Fischer, C. *Quantum non-demolition readout for optically trapped alkaline-earth Rydberg atoms* PhD thesis (ETHz, 2022).
13. Muni, A. *et al.* Optical coherent manipulation of alkaline-earth circular Rydberg states. *Nature Physics* **18,** 502–505 (2022).
14. Bluvstein, D. *et al.* Logical quantum processor based on reconfigurable atom arrays. *Nature* **626,** 58–65 (2024).
15. Nogrette, F. *et al.* Single-atom trapping in holographic 2D arrays of microtraps with arbitrary geometries. *Physical Review X* **4,** 021034 (2014).
16. W.Goodman, J. *Introduction to Fourier Optics* 3rd edtion (Ben Roberts, 2004).
17. Konzett, L. *Array of optical bottle beams using a liquid-crystal spatial light modulator* Available at: `https://tiqi.ethz.ch/publications-and-awards/masters-theses.html`. Master's thesis (ETHz, 2023).

18. Hecht, E. *Optics* 5th edtion (Pearson Education Limited, 2016).
19. Smith., T. T. Spherical aberration in thin lenses. *Scientific Papers of the Bureau of Standards* **18,** 559–584 (1922).
20. MEETOPTICS. *Optical Aberrations* `https://www.meetoptics.com/academy/optical-aberrations` (2024).
21. Smith, W. J. *Modern optical engineering* 3rd edtion (McGraw-Hill, 2000).
22. Colm McAlinden Mark McCartney, J. M. Mathematics of Zernike polynomials: a review. *Clinical and Experimental Ophthalmology* **39,** 820–827 (2011).
23. Fritz, Z. Begungstheorie des Schneidenvereahrens und seiner verbesserten Form der Phasenkontrastmethods. *Physica* **1,** 689 (1934).
24. Vasudevan Lakshminarayanan, A. F. Zernike polynomials: a guide. *Journal of Modern Optics* **58 (7),** 545–561 (2011).
25. Niu, K. & Tian, C. Zernike polynomials and their applications. *Journal of Optics* **24,** 123001 (2022).
26. Slmsuite Developers. *slmsuite: a Python package for high-precision spatial light modulator (SLM) control and holography* `https://slmsuite.readthedocs.io`. 2024.
27. Meadowlark Optics, I. *1920 HDMI User Manual*
28. O'Callaghan, M. J. Influence of SLM pixel size and shape on the performance of optical correlators and optical memories. *Proceedings of the SPIE* **4089,** 198–207 (2000).
29. Meadowlark Optics, I. *Spatial Light Modulator – 1920×1200 data sheet*
30. Harriman, J., Linnenberger, A., Serati, S., *et al.* Improving spatial light modulator performance through phase compensation. *Proceedings of SPIE—The International Society for Optical Engineering* **5553,** 58–67 (2004).
31. López-Quesada C Andilla J, M.-B. E. Correction of aberration in holographic optical tweezers using a Shack-Hartmann sensor. *Applied Optics* **48(6),** 1084–1090 (2009).
32. C. Kohler, F. Z. & Osten, W. Characterization of a spatial light modulator and its application in phase retrieval. *Applied Optics* **48(20),** 4003–4008 (2009).
33. Tomáš Čižmár, M. M. & Dholakia, K. In situ wavefront correction and its application to micromanipulation. *Nature Photonics* **4,** 388–394 (2010).
34. Thorlabs. *BC207 and BC210C Series Camera Beam Profiler Manual*
35. Suzaki, Y. & Tachibana, A. Measurement of the m sized radius of Gaussian laser beam using the scanning knife-edge. *Applied Optics* **14(12),** 2809–2810 (1975).
36. Rashad, M. M. *Measurements of Laser Beam Using Knife Edge Technique* MA thesis (Politecnico di Milano, 2019).
37. MILONNI, P. W. & EBERLY, J. H. *LASER PHYSICS* (John Wiley Sons, Inc., 2010).

38. Siegman, A. E. *How to (Maybe) Measure Laser Beam Quality* Tutorial presented at Optical Society of America Annual Meeting Long Beach, California. 1997.

Eidgenössische Technische Hochschule Zürich
Swiss Federal Institute of Technology Zurich

Declaration of originality

The signed declaration of originality is a component of every written paper or thesis authored during the course of studies. In consultation with the supervisor, one of the following three options must be selected:

- (●) I confirm that I authored the work in question independently and in my own words, i.e. that no one helped me to author it. Suggestions from the supervisor regarding language and content are excepted. I used no generative artificial intelligence technologies[1].
- ( ) I confirm that I authored the work in question independently and in my own words, i.e. that no one helped me to author it. Suggestions from the supervisor regarding language and content are excepted. I used and cited generative artificial intelligence technologies[2].
- ( ) I confirm that I authored the work in question independently and in my own words, i.e. that no one helped me to author it. Suggestions from the supervisor regarding language and content are excepted. I used generative artificial intelligence technologies[3]. In consultation with the supervisor, I did not cite them.

Title of paper or thesis:

Design and Implementation of an Optical Tweezer Setup for Calcium Atoms

Authored by:
If the work was compiled in a group, the names of all authors are required.

Last name(s):	First name(s):
Qianlong	HE

With my signature I confirm the following:

- I have adhered to the rules set out in the Citation Guide.
- I have documented all methods, data and processes truthfully and fully.
- I have mentioned all persons who were significant facilitators of the work.

I am aware that the work may be screened electronically for originality.

Place, date	Signature(s)
Zürich, 18/10/2024	何千龙

If the work was compiled in a group, the names of all authors are required. Through their signatures they vouch jointly for the entire content of the written work.

[1] E.g. ChatGPT, DALL E 2, Google Bard
[2] E.g. ChatGPT, DALL E 2, Google Bard
[3] E.g. ChatGPT, DALL E 2, Google Bard